

University of Alabama in Huntsville

**LOUIS**

---

Theses

UAH Electronic Theses and Dissertations

---

2024

## The impact of the 2018 camp fire on land-atmosphere interactions

Andrew C. Blackford

Follow this and additional works at: <https://louis.uah.edu/uah-theses>

---

### Recommended Citation

Blackford, Andrew C., "The impact of the 2018 camp fire on land-atmosphere interactions" (2024).

*Theses*. 658.

<https://louis.uah.edu/uah-theses/658>

This Thesis is brought to you for free and open access by the UAH Electronic Theses and Dissertations at LOUIS. It has been accepted for inclusion in Theses by an authorized administrator of LOUIS.

**THE IMPACT OF THE 2018 CAMP FIRE ON LAND-ATMOSPHERE  
INTERACTIONS**

**Andrew C. Blackford**

**A THESIS**

**Submitted in partial fulfillment of the requirements  
for the degree of Master of Science  
in  
The Department of Atmospheric and Earth Science  
to  
The Graduate School  
of  
The University of Alabama in Huntsville  
May 2024**

**Approved by:**

Dr. Udaysankar Nair, Research Advisor  
Dr. Sundar Christopher, Committee Member  
Dr. John Christy, Committee Member  
Dr. Aaron Kaulfus, Committee Member  
Dr. Lawrence Carey, Department Chair  
Dr. Rainer Steinwandt, College Dean  
Dr. Jon Hakkila, Graduate Dean

## **Abstract**

# **THE IMPACT OF THE 2018 CAMP FIRE ON LAND-ATMOSPHERE INTERACTIONS**

**Andrew C. Blackford**

**A thesis submitted in partial fulfillment of the requirements  
for the degree of Master of Science**

**Atmospheric and Earth Science**

**The University of Alabama in Huntsville  
May 2024**

Research on the effects of wildfire-induced changes in land use and land cover (LULC) on atmospheric processes is limited. This thesis presents a thorough analysis using satellite remote sensing and numerical modeling to examine how land-atmosphere interactions have been altered by the burn scar from the 2018 Camp Fire event in California. Satellite data reveals significant changes in surface characteristics affecting land-atmosphere interactions, such as land cover type, vegetation fraction (-0.12), albedo (+0.01), daytime temperature (+2.5 K), and roughness length (>-90%). Numerical modeling, based on satellite-derived LULC change scenarios, indicates notable shifts in net radiation (-0.2 MJ m<sup>-2</sup>), sensible heat flux (+15Wm<sup>-2</sup>), diurnal temperature range (+5%), mesoscale circulation patterns, and rainfall patterns. The influence on cloud formation and rainfall is heightened by the fire scar's occurrence in complex terrain, with implications for water resource management and assessing drought-flood risks in fire-prone areas.



## Acknowledgements

First and foremost, all glory is given to God. I am nothing without Him, and He has led me through this experience in its entirety. He has blessed me with the abilities to produce this study in a timely manner, and I thank Him every day for who I am. God is good, all the time! “For I am sure that neither death nor life, nor angels nor rulers, nor things present nor things to come, nor powers, nor height nor depth, nor anything else in all creation, will be able to separate us from the love of God in Christ Jesus our Lord!” (Romans 8:38-39, ESV)

I must also thank my family for their unwavering support in this journey through graduate school. Since applying to graduate school in the fall of 2021, they have been there by my side encouraging me, and I am truly grateful. I also want to thank my professors at both Valparaiso University and UAH, as they have given me the knowledge and skills that I needed to complete this work. A special thank you is given to Dr. Nair, my research advisor, for his excellent guidance at every step of this process. Additionally, I would like to thank my committee members Dr. Christopher, Dr. Christy, and Dr. Kaulfus for their input and guidance in this research endeavor- this work in a more complete state because of your help.

Likewise, I must thank all of my wonderful friends and colleagues who have known me either for a couple of months or for life. From the time that I was 12 years old, I knew I had a passion for the atmospheric sciences, and I am very appreciative of all of your encouragement and steadfastness in being with me through this journey to get to where I am today.

Finally, I am grateful and thankful for the funding that made all of this work possible. Exploratory analysis that provided motivation for this research is the NASA Interagency Implementation and Advanced Concepts Team (IMPACT) Visualization, Exploration, and Data

Analysis (VEDA) data discovery story entitled “Wildfires Affect Local Weather, Climate, and Hydrology”. This project was funded by NASA Grant #80MSFC22M0004.

# Table of Contents

<b>Abstract.....</b>	<b>ii</b>
<b>Acknowledgements .....</b>	<b>iv</b>
<b>Table of Contents .....</b>	<b>vi</b>
<b>List of Figures.....</b>	<b>viii</b>
<b>List of Tables .....</b>	<b>x</b>
<b>List of Acronyms .....</b>	<b>xi</b>
<b>List of Symbols .....</b>	<b>xiv</b>
<b>Chapter 1. Introduction .....</b>	<b>1</b>
1.1 Introduction and Purpose .....	1
1.2 Previous Studies .....	2
1.3 The Impacts of the 2018 Camp Fire.....	4
1.4 Research Questions and Hypotheses.....	5
<b>Chapter 2. Data .....</b>	<b>8</b>
2.1. Satellite Remote Sensing Observations .....	8
2.2. 3D WRF ARW .....	11
<b>Chapter 3. Methods .....</b>	<b>12</b>
3.1. Satellite Analysis Methodology .....	12
3.2. 3D WRF ARW Methodology.....	14
<b>Chapter 4. Results and Discussion .....</b>	<b>19</b>
4.1. Satellite Remote Sensing Results.....	19
4.2. 3D WRF ARW Results .....	24
4.2.1. Modeled Changes in Land Surface Properties .....	25
4.2.2. Modeled Changes in the Local Surface Energy Balance .....	30

4.2.3. Modeled Changes in Local Boundary Layer Features .....	38
4.2.3.1. Temperature and Moisture .....	38
4.2.3.2. PBLH, LCL, and LFC .....	43
4.2.3.3. Wind and Mesoscale Circulations .....	45
4.2.4. Modeled Changes in Cloud Forcing and Precipitation.....	52
<b>Chapter 5. Conclusions.....</b>	<b>59</b>
<b>References .....</b>	<b>63</b>
<b>Appendix A. Statistical Overview of WRF Simulation Results.....</b>	<b>72</b>
<b>Appendix B. WRF Simulation Average U-Wind Perturbations .....</b>	<b>74</b>

## List of Figures

<b>Figure 3.1:</b> NLCD LULC classifications over the burn scar domain for 2016 and 2019 (pre and post-fire).....	13
<b>Figure 3.2:</b> Green fraction and NLCD classification maps for the innermost WRF domain .....	15
<b>Figure 3.3:</b> Study domain of the 3D WRF ARW simulations. The Camp Fire burn scar is located at the center of the innermost domain. ....	16
<b>Figure 4.1:</b> Pre-fire subtracted from post-fire three-year monthly mean differences of a) LST Day, b) LST Night, c) NDVI, and d) Albedo WSA over the Camp Fire burn scar domain.....	21
<b>Figure 4.2:</b> Monthly mean spatially-averaged time series across the Camp Fire burn scar extent for Day LST, Night LST, NDVI, and Albedo WSA (black lines).....	22
<b>Figure 4.3:</b> Run-averaged spatial difference plot of albedo, averaged across one diurnal cycle, subset to domain 3 of the WRF simulations .....	26
<b>Figure 4.4:</b> Run-averaged, spatial difference plots of LST from domain 3 of the WRF output..	28
<b>Figure 4.5:</b> Time series analysis of WRF output LST for the spatially-averaged burn scar extent. Pre- and post-fire LULC WRF simulations are both shown.....	29
<b>Figure 4.6:</b> Run-averaged, spatial difference plots of latent heat and sensible heat fluxes over WRF domain 3, averaged over a 24-hour diurnal cycle from 13-13 UTC.....	33
<b>Figure 4.7:</b> Run-averaged, spatial difference plots of the total net radiation over WRF domain 3, averaged over a 24-hour diurnal cycle from 13-13 UTC.....	35
<b>Figure 4.8:</b> Time series analysis of WRF output net radiation for a) the spatially-averaged burn scar extent, and b) at Buck's Lake. Pre- and post-fire simulations are both shown .....	36
<b>Figure 4.9:</b> Burn scar-averaged difference meteograms of the local energy budget .....	38
<b>Figure 4.10:</b> Maximum, minimum, and mean 2-meter temperature across domain 3 of the WRF output for all case days, as well as the maximum, minimum, and mean differences .....	40
<b>Figure 4.11:</b> 24-hour time-height plots illustrating the interaction between temperature, moisture, and the PBLH.....	43
<b>Figure 4.12:</b> Run-averaged time series analysis of PBLH, LCL, and LCL deficit, spatially averaged over the Camp Fire burn scar extent.....	45
<b>Figure 4.13:</b> Run-averaged time-height plot at Paradise, CA of the difference in total wind post-fire compared to pre-fire. ....	47

<b>Figure 4.14:</b> Run-averaged latitudinal cross sections and 10-meter x-y spatial difference plots of the u and v components of wind as well as the total wind.....	<b>51</b>
<b>Figure 4.15:</b> Run-averaged, spatial difference plots of the friction velocity over WRF domain 3, averaged over a 24-hour diurnal cycle from 13-13 UTC.....	<b>52</b>
<b>Figure 4.16:</b> Run-averaged mean spatial difference plots of low, middle, and high cloud layer fraction .....	<b>56</b>
<b>Figure 4.17:</b> Example WRF convective case date showing the pre-fire and post-fire accumulated rainfall footprints, as well as the difference post-fire compared to pre-fire .....	<b>57</b>
<b>Figure B.1:</b> x-z cross section analysis of run-averaged u-wind perturbations. Each hour of the diurnal cycle is shown for the innermost WRF domain. ....	<b>75</b>

## List of Tables

<b>Table 4.1.1:</b> Selected case dates simulated using the WRF ARW, listed alongside the general conditions of the 36-hour period from 12 UTC on the case date to 18 UTC the next day .....	<b>16</b>
<b>Table 4.1.2:</b> Sensitivity analysis results for KOAK and KCIC. The values are reported as RMSE / MBE / ME.....	<b>18</b>
<b>Table 4.1:</b> Mean, Maximum, and Minimum values of MODIS-derived variables examined pre-fire, post-fire, and the difference between post- and pre-fire, subset to the burn scar extent.	<b>20</b>
<b>Table 4.2:</b> Pre-and post-fire statistical analysis of MODIS-derived variables examined over the Camp Fire burn scar extent from 2002-2022. ....	<b>23</b>
<b>Table A.1</b> Computed statistical results for a selection of variables examined from modeled WRF output.....	<b>73</b>

## List of Acronyms

<b>Acronym</b>	<b>Description</b>
AET	Afternoon-Evening Transition
AGL	Above Ground Level
AHPS	Advanced Hydrologic Prediction Service
ARW	Advanced Research WRF
ASOS	Automated Surface Observing Systems
BMJ	Betts-Miller-Janjic
BRDF	Bidirectional Reflectance Distribution Function
CA	California
CONUS	Contiguous United States
CU	Cumulus Parameterization
DALR	Dry Adiabatic Lapse Rate
DTR	Diurnal Temperature Range
EEPS	E- $\epsilon$ Parameterization Scheme
FA	Free Atmosphere
FEDS	Fire Event Data Suite
FRP	Fire Radiative Power
GEDI	Global Ecosystem Dynamics Investigation
GF	Grell-Freitas
GLAS	Geoscience Laser Altimeter System
HLS	Harmonized Landsat and Sentinel-2
HRRR	High-Resolution Rapid Refresh
KCIC	Chico, California ASOS Site

KF	Kain-Fritsch
KOAK	Oakland, California ASOS Site
LCL	Lifted Condensation Level
LE	Latent Heat Flux
LFC	Level of Free Convection
LiDAR	Light Detection and Ranging
LST	Land Surface Temperature
LULC	Land Use – Land Cover
MALR	Moist Adiabatic Lapse Rate
MBE	Mean Bias Error
ME	Maximum Error
MISR	Multi-angle Imaging Spectroradiometer
MODIS	Moderate Resolution Imaging Spectrometer
MRLC	Multi Resolution Land Characteristics
MSI	Multi-Spectral Instrument
MTBS	Monitoring Trends in Burn Severity
MYNN3	Mellor-Yamada Nakanishi and Niino Level 3
NASA	National Aeronautics and Space Administration
NBL	Nocturnal Boundary Layer
NCAR	National Center for Atmospheric Research
NDVI	Normalized Difference Vegetation Index
NIR	Near-Infrared
NLCD	National Land Cover Database
NOAA	National Oceanic and Atmospheric Administration
NOAH LSM	Noah-Oregon State University Land Surface Model

NPP	National Polar-orbiting Partnership
OLI	Operational Land Imager
PBL	Planetary Boundary Layer
PBLH	Planetary Boundary Layer Height
PG&E	Pacific Gas and Electric
QPF	Quantitative Precipitation Forecast
RMSE	Root Mean Square Error
SH	Sensible Heat Flux
US	United States
USD	United States Dollars
UTC	Universal Time Coordinated
VIIRS	Visible Infrared Imaging Radiometer Suite
WSA	White Sky (Albedo)
WRF	Weather Research and Forecasting
YSU	Yonsei University

## List of Symbols

<b>Symbol</b>	<b>Definition</b>
CFRAC	Cloud Fraction
$c_p$	Specific Heat of Air at Constant Pressure
$E$	Rate of Ongoing Phase Change
$e$	Vapor Pressure
$e_s$	Saturation Vapor Pressure
$L$	Latent Heat
$S_0$	Solar Constant
$P$	Atmospheric Pressure
$R_{net}$	Net Radiation
RH	Relative Humidity
$Q_{in}$	Total Incoming Radiation
$Q_{out}$	Total Outgoing Radiation
$T$	Temperature
$T_d$	Dewpoint Temperature
$T_{parcel}$	Temperature of Air Parcel
$\Delta T$	Change in Surface vs. Air Temperature
$U$	Instantaneous Wind
$U'$	Wind Perturbation
$\bar{U}$	Mean Wind
$u$	u-Component of Wind
$u^*$	Friction Velocity
$V$	Total Wind

$v$	v-Component of Wind
WDIR	Wind Direction
WSPD	Wind Speed
$z$	Height Above Ground Level
$z_0$	Roughness Length
$\alpha$	Planetary Albedo
$\varepsilon$	Emissivity
$\Gamma_d$	Dry Adiabatic Lapse Rate
$\Gamma_{env}$	Environmental Lapse Rate
$\Gamma_m$	Moist Adiabatic Lapse Rate
$\kappa$	Von Kármán Constant
$\rho$	Air Density
$\sigma$	Stefan-Boltzmann Constant

*The trees wave their arms and the clouds try to plead  
Desperately yelling out there's something else in this world that we need  
And it happens to be free*

– Tyler Joseph

## Chapter 1. Introduction

### 1.1 Introduction and Purpose

There has been substantial research establishing connections between land use-land cover (LULC) and local weather and climate patterns (Charney 1975; Pielke and Avissar 1990; Santanello *et al.* 2018). These connections manifest through pathways like modifications to the surface energy budget, changes to sensible and latent heat fluxes, and alterations to surface roughness. Surface parameters, including emissivity, albedo, soil moisture, and vegetation cover, play crucial roles in controlling these pathways. Often, LULC change occurs at large scales over an extended period of time (*e.g.*, urbanization) with a corresponding temporal response from the atmosphere. Wildfires, however, cause drastic reductions in vegetation and can char the soil rapidly. The resultant “burn scars” are thus a shock to the land-atmosphere system from which the local environment progressively recovers. Further, wildfires burn hundreds of thousands of acres annually in the United States alone, and trends in burned area and wildfire frequency have been increasing since 1984 (Eidenshink *et al.* 2007; Cochrane *et al.* 2012). However, historical evidence challenges the notion of unparalleled trends by revealing that approximately 1,800,000 hectares of California wildlands burned annually prior to 1800 (Stephens *et al.* 2007). Additionally, modifications to policy have been enacted in the Western United States to curtail suppression tactics, facilitating the integration of wildland fire as an essential ecological process and natural change agent in both land use planning and fire management programs (Franco and Úbeda 2021).

Against this backdrop, this study aims to comprehensively investigate the impacts of drastic LULC changes resulting from the 2018 Camp Fire that devastated the city of Paradise, California. While extensive research has been conducted on the connections between LULC and

local weather and climate patterns, there is a significant gap in understanding the specific effects of sudden severe vegetation removal on the energy balance, mesoscale circulations, and cloud and precipitation forcing at a localized level. This study aims to address this knowledge gap by focusing on the aftermath of the 2018 Camp Fire and seeks to answer three key questions by testing three hypotheses that delve into the specific mechanisms and consequences of the observed LULC changes following the wildfire (Section 1.4.).

By rigorously examining the alterations to the land surface properties, local energy budget, boundary layer features, and cloud and precipitation forcing, this research aims to contribute valuable insights into the intricate interactions between wildfires, land-atmosphere dynamics, and subsequent local weather patterns. The findings are expected to enhance understanding of the broader implications of rapid LULC changes caused by wildfires, providing valuable knowledge for land management, weather and climate modeling, and disaster mitigation efforts.

## **1.2 Previous Studies**

Several prior studies have demonstrated that areas affected by wildfire burn scars exhibit reduced vegetation, darkening of the soil surface, and drying of subsurface soil layers due to the burning process (Hubbert *et al.* 2012; Parise and Cannon 2012; Williams *et al.* 2015). These changes in vegetation and soil properties are well known to leave burn scars more susceptible to flooding and erosion compared to an undisturbed environment, even for comparable rainfalls (Debano; Cannon *et al.* 2001; Cannon and DeGraff 2009; Chen *et al.* 2020; DiBiase and Lamb 2020; Fan *et al.* 2017; Gartner *et al.* 2014; Hubbert *et al.* 2012; May and Gresswell 2004; Parise and Cannon 2012; Prochaska *et al.* 2008; Dennis Staley *et al.*; Staley *et al.* 2017; Takahashi; United States Geological Survey 2020). Vegetation loss and soil darkening also principally lower

albedo and emissivity, which in turn modifies the surface energy budget and increases surface temperature (Chen *et al.* 2001; Hernandez *et al.* 2015; Knowles 1993; Molders and Kramm 2007; Page 2007; Tryhorn *et al.* 2008). With the loss of vegetation, the Bowen Ratio – which is the ratio of sensible heat flux to latent heat flux - also increases, further contributing to the increase in surface temperatures over the burn scar relative to the surrounding unburned area (Chen *et al.* 2001; Molders and Kramm 2007; Page 2007; Tryhorn *et al.* 2008). This reduced vegetation coverage (particularly the loss of tree canopy) results in lower surface drag and friction velocity over the burn scar. Such localized changes in land surface properties can drive mesoscale circulations and enhance boundary layer thermal updraft strength (Hernandez *et al.* 2015; Page 2007; Souza *et al.* 2000). More generally, temperature gradients between vegetation and bare ground induce mesoscale circulations similar in structure to the nonclassical land-sea breeze mesoscale circulation (Anthes 1984; McCumber 1980; McPherson 2007; Ookouchi Y. *et al.* 1984; Pielke and Avissar 1990; Segal *et al.* 1988, 1992).

The impacts of mesoscale circulations are far-reaching, influencing several aspects of the local weather and climate patterns. Mesoscale circulations can alter the depth of the planetary boundary layer (PBL) (Souza *et al.* 2000) and shift local wind patterns (Silva Dias 1996; Souza *et al.* 2000; Renno, *et al.* 1998). Though not covered in this study, convergence zones associated with the local wind shifts under mesoscale circulations have been found to influence convective initiation (Barthlott *et al.* 2006) as well as pollution transport (Pielke *et al.* 1991). These circulations also can alter the magnitude and sign of the moisture flux, which in turn impact cloud cover and precipitation footprints (Anthes 1984; Souza *et al.* 2000; Renno and Ingersoll 1996). Subsequently, the establishment of mesoscale circulations in specific locations, along with the intensity of these circulations, can have cascading effects on local agricultural practices

(Rabin *et al.* 1990), ecology (Cutrim *et al.* 1995), and air quality (Pielke *et al.* 1991; McNider and Pour-Biazar 2020) of the region in question. However, the intensity of such circulations is reliant on the structure of the PBL in relation to heat and energy transfer as well as the state of surface baroclinic zones, where temperature gradients exist along a constant pressure surface (De Wekker and Kossmann 2015; Souza *et al.* 2000) Having highlighted the diverse impacts of mesoscale circulations, it is noteworthy that a large gap in research currently exists concerning the effects of LULC changes on the surface energy budget and how that response impacts mesoscale circulations.

### **1.3 The Impacts of the 2018 Camp Fire**

The devastating Northern California ‘Camp Fire’ occurred from November 8<sup>th</sup>-25<sup>th</sup>, 2018, burning over 153,000 acres and causing \$16.65 billion (2018 USD) in damages. The Camp Fire began from a faulty Pacific Gas and Electric (PG&E) transmission line, and resulted in 85 fatalities and 17 injuries. The Camp Fire was the most expensive natural disaster in the world in 2018, and remains the 7<sup>th</sup> deadliest wildfire in U.S. history as of 2023. A striking 95% of the city of Paradise, CA was destroyed, and 18,804 buildings were destroyed by the fire (Brewer and Clements 2020; Mass and Ovens 2021; Lizzie Johnson 2021).

The repercussions of the 2018 Camp Fire extended beyond the immediate impacts of acres burned and financial losses. Evacuation efforts were marred by the fire's rapid spread, leading to challenging conditions for residents attempting to escape. The immense volume of smoke generated by the wildfire had far-reaching consequences on air quality, affecting millions and prompting health warnings across Northern California (Chow *et al.* 2022; Rooney *et al.* 2020; Simms *et al.* 2021). Emergency responders, including firefighters from various jurisdictions, worked diligently to contain the fire, rescue stranded individuals, and provide aid to

those affected. The disaster's impact went beyond physical destruction, manifesting in profound social and psychological consequences for the affected communities, with the displacement of thousands and the loss of several communities (Spearing and Faust 2020; Schulze *et al.* 2020; Knapp *et al.* 2021). Moreover, the Camp Fire had severe environmental consequences, influencing the local ecosystem's health, soil quality, and water systems. In the aftermath, legal and regulatory scrutiny intensified, particularly targeting PG&E. This wildfire was also a huge instigator of debates on wildfire prevention, utility infrastructure maintenance, and liability issues in the face of mounting wildfire risks in California.

The Camp Fire thus stands as a complex and tragic event, underscoring the need for a holistic understanding of its impacts beyond the immediate physical devastation. Given the sheer scale and profound consequences of this tragic event, investigating the modifications of local weather and climate resulting from this substantial LULC change becomes not only scientifically pertinent but also crucial for informing future disaster resilience strategies.

#### **1.4 Research Questions and Hypotheses**

In contrast to the many studies focusing on the impacts of burn scars regarding erosion and runoff, there have been comparatively few studies that focus on the impacts of LULC changes on the surface energy budget response, mesoscale circulations, and cloud and precipitation forcing. Thus, this thesis will focus on the LULC change-driven impacts stemming from the 2018 Camp Fire that devastated Paradise, California. This thesis thus seeks to answer the following questions:

1. How does severe removal of vegetation impact the local surface energy balance?

2. What are the impacts of drastic changes in LULC to localized mesoscale circulation development?
3. What are the downstream effects on cloud formation and precipitation footprints as a result of localized yet drastic LULC changes?

To answer these questions, the following three hypotheses are tested:

H1. The removal of the tree canopy as a result of the 2018 Camp Fire will lead to increased LST and decreased moisture, thereby increasing the Bowen Ratio and altering both the local radiation budget and energy balance.

H2. The changes in the surface sensible heat flux and temperature gradients will drive a noteworthy nonclassical mesoscale circulation along the perimeter of the Camp Fire burn scar.

H3. The reduction of vegetation cover will result in a surface roughness gradient along burned and unburned regions that enhances convergence, thus resulting in enhanced convective updrafts downwind of the burn scar, thereby increasing cloud cover and precipitation formation.

This thesis utilizes a data synthesis approach combining satellite remote sensing data and numerical modeling experiments to investigate these impacts. The manuscript will be laid out as follows: Chapter 2 discusses the datasets acquired and utilized in testing the three hypotheses, Chapter 3 lays out the methodology of the hypothesis testing, Chapter 4 discusses the results that were discovered and their implications, and Chapter 5 summarizes the overall conclusions of this

work. This manuscript is being prepared for submission to the *Bulletin of the American Meteorological Society*.

## Chapter 2. Data

Two main types of data were utilized in this study to most wholly capture the impacts of burn scars on local weather and climate patterns. Satellite-remote sensing datasets used in this study will be discussed in section 2.1 and numerical modeling experiments will be discussed in section 2.2.

### 2.1. Satellite Remote Sensing Observations

In this investigation, the impact of LULC change and the associated alterations to land surface and meteorological properties across the burn scar domain were primarily examined using the National Land Cover Database (NLCD) and the Moderate Resolution Spectroradiometer (MODIS) sensor aboard the National Aeronautics and Space Administration's (NASA) Aqua and Terra satellites.

The NLCD data employed in this research were extracted from Landsat satellite measurements captured in 2016 and 2019, offering a 30-meter resolution for comparing conditions before and after the wildfire occurred. It is important to note that the NLCD is organized through the Multi Resolution Land Characteristics (MRLC) consortium, a collaborative effort of federal agencies providing land cover information for the United States (Homer and Hossain 2007; Homer *et al.* 2012; Homer and Yang 2015). The 2016 and 2019 data were employed to quantify LULC changes in a manner akin to the approach delineated by Homer *et al.*, 2015.

Regarding the MODIS Terra and Aqua satellite data, the analysis incorporated the LST Day and Night, Normalized Difference Vegetation Index (NDVI), and White Sky Albedo (WSA

Albedo) products. Both MODIS Terra and Aqua operate on a sun-synchronous orbit, passing over the burn scar daily at 10:30 AM and 1:30 PM local time.

The LST Day and Night products are available at a spatial resolution of 1 km and are composited over 8 days (MOD11A2). The computation of LST is based on a split-window algorithm that extracts information from MODIS channels 31 and 32, which have central wavelengths of 11.03 and 12.02  $\mu\text{m}$ , respectively (Wan *et al.* 2002). Despite an average error of 2.0 K with an approximate 0.5 K standard deviation, this dataset remains a reliable estimation of LST in the burn scar domain during the study period (Wan 2014).

The study also leveraged the NDVI product, which offers a spatial resolution of 250 m and a 16-day temporal composite product (MOD13Q1). Computed using the near-infrared (nir) and red reflectance channels, the NDVI values range between -1 and 1, serving as a reliable proxy for assessing healthy vegetation cover for each pixel (Didan and Barreto Munoz 2015).

The MODIS Bidirectional Reflectance Distribution Function (BRDF)/Albedo product equipped for this study integrates data from MODIS and Multi-angle Imaging Spectroradiometer (MISR) instruments to derive surface albedo. The WSA albedo variable was utilized from this product, which is obtained by integrating the BRDF over all viewing and irradiance directions. Notably, these measures are unaffected by atmospheric conditions, making them valuable for climate models. It utilizes the RossThick-LiSparse model, along with a simple polynomial for solar-zenith angle dependence, and band-dependent weighting factors for spectral-to-broadband conversion, contributing to the derivation of actual albedo. These data, available in varying scales, are crucial for global and regional climate modeling, and also has implications on the energy flux at the surface and into the PBL (Strahler and Muller 1999). All four of these MODIS datasets were examined over the extensive time span of 2015-2022.

In addition to the MODIS satellite data, the Harmonized Landsat and Sentinel-2 (HLS) product constructed by NASA was utilized for examining high-resolution visible satellite imagery of the recovery of vegetation post-burn scar. HLS is a 30-meter spatial resolution product created by harmonizing the reflectance data collected by Landsat 8/9's Operational Land Imager (OLI) and Sentinel-2's Multi-Spectral Instrument (MSI). The temporal resolution is dependent upon the number of satellites in the virtual constellation, but is currently 3 days or less with Landsat 8/9 and Sentinel-2A/B in orbit. HLS was preferred to only Landsat or Sentinel-2 data due to the increased temporal resolution provided by harmonizing the data retrievals from the OLI and MSI instruments. HLS data production takes Level-1 observations from Landsat and Sentinel-2 scenes, applies atmospheric correction, cloud masking, BRDF normalization, and a band pass filter to match Sentinel-2 surface reflectance to that of Landsat (Claverie *et al.* 2018).

Finally, in order to examine the fast propagation of the fire perimeter, the Visible Infrared Imaging Radiometer Suite (VIIRS)-derived Fire Event Data Suite (FEDS) was examined. The FEDS algorithm tracks fire movement and severity by ingesting observations from the VIIRS thermal sensors on the Suomi National Polar-Orbiting Partnership (NPP) and National Oceanic and Atmospheric Administration (NOAA)-20 satellites. This algorithm uses raw VIIRS observations to generate a polygon of the fire, locations of the active fire line, and estimates of the mean Fire Radiative Power (FRP). The VIIRS sensors overpass at approximately 1:30 AM and PM local time, and thus provide estimates of fire evolution approximately every 12 hours. The data produced by this algorithm describes where spatial patterns of active fires reside and how fires evolve through time. This Contiguous United States (CONUS)-wide implementation of the FEDS algorithm is based on Chen *et al.* 2022's algorithm for California.

## 2.2. 3D WRF ARW

Version 4.3 of the 3-dimensional Weather Research and Forecasting (WRF) - Advanced Research WRF (ARW) dynamical core model was utilized extensively in this study. The 3D WRF is a limited-area, fully-compressible, non-hydrostatic model designed specifically for research endeavors in the atmospheric sciences. The WRF ARW uses the Arakawa C-grid horizontal staggering method for its horizontal grid (Arakawa and Lamb 1977; Purser and Leslie 1988) and uses a terrain-following, mass-based, hybrid sigma-pressure vertical coordinate system. Its simulation capacity supports spatial resolutions ranging from coarse global data to high-resolution large-eddy simulations. It contains an array of user-flexible physics parameterization schemes and dynamic options for ease of hypothesis testing in atmospheric research. Additionally, the Noah-Oregon State University Land Surface Model (NOAH LSM) was implemented to examine the energy budget of the surface and atmosphere in this study (Sridhar *et al.* 2002).

## **Chapter 3. Methods**

The methodology of the analysis of satellite remote sensing data and atmospheric modeling data used in this research has been laid out in sections 3.1 and 3.2 below. It should be noted that the outline of the burn scar, essential for the spatial analysis in this study, was derived from the Monitoring Trends in Burn Severity (MTBS) dataset.

### **3.1. Satellite Analysis Methodology**

In examining the NLCD LULC classifications across the burn scar domain in 2016 compared to 2019, it was clear that the primary LULC classifications within the burn scar perimeter pre-fire were evergreen forest and shrubbery cover, while the dominant classifications post-fire were grassland and barren land. However, outside of the burn scar perimeter there were no noteworthy LULC changes between the two time periods. These changes in LULC across the burn scar domain were then compared to the differences of each MODIS product post-wildfire subtracted from pre-wildfire to compare spatial distributions of the differences in tandem with the LULC changes.

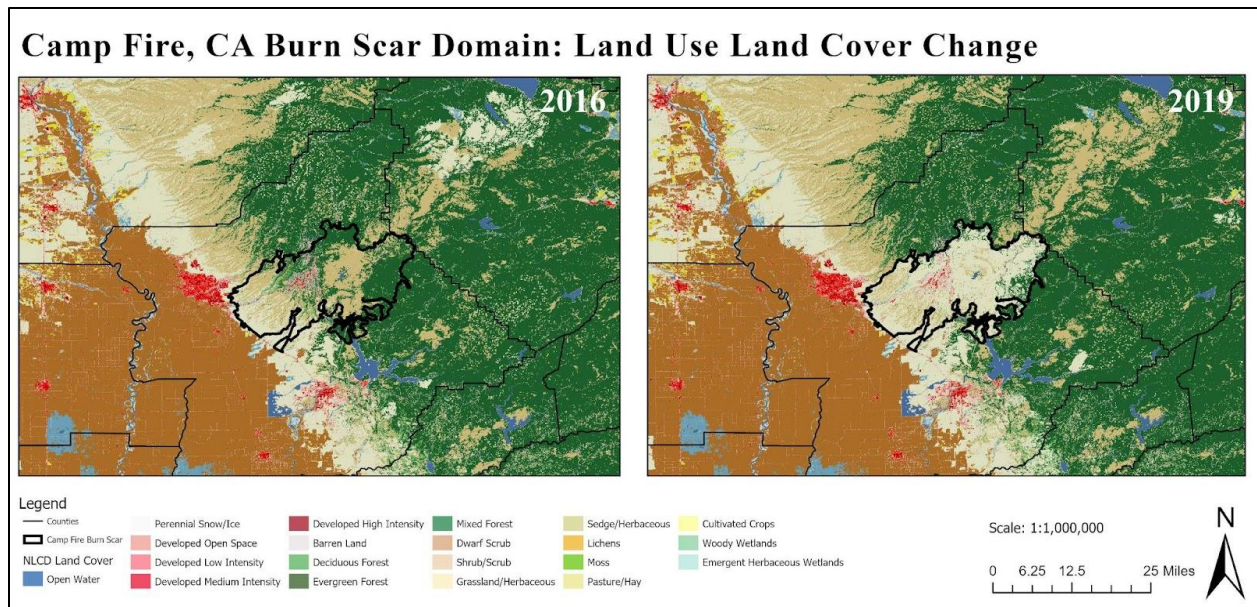


**Figure 3.1:** NLCD LULC classifications over the burn scar domain for 2016 and 2019 (pre- and post-fire). The thick black outline is the MTBS-designated burn scar extent.

In order to examine how the resultant burn scar from the wildfire case study impacted the changes in surface properties, the MODIS-derived LST Day, LST Night, NDVI, and WSA albedo were all utilized. A six-year period of January 2015 to December 2022 was obtained for each of the four MODIS products. This temporal range was chosen due to the active period of the Camp Fire being located approximately in the middle of the period. Each product has different spatial resolutions and temporal latencies (section 2), so all products were re-gridded to 1 km and averaged by month. These monthly spatial maps of each product were then averaged over the burn scar domain across the three years before the fire (2015-2018) and three years after the fire (2019-2022) to analyze the perceived impact of the burn scar compared to a control state. Spatial difference maps were then created from the post- compared to pre-fire monthly mean values. In addition, spatially-averaged 20-year time series (2002-2022) of each of the four products were computed using the monthly averaged data, and seasonal decomposition was performed. From the seasonal decomposition, the decomposed trend was extracted and analyzed.

The Mann-Kendall statistical test was then applied to these trends in order to determine if any were monotonic and statistically significant. It should also be acknowledged that in computing the monthly spatial averages of LST, the Hu and Brunsell (2013) methodology of minimizing cloud contamination was applied.

Additionally, the channels centered on 0.48 (Blue), 0.56 (Green), 0.65 (Red), and 0.83 (nir) microns from HLS tile 10SFJ were utilized in this study across a multi-year range of January 2017 to December 2022 to examine the vegetation recovery over the burn scar perimeter. These scenes were pulled using checks to ensure at least 70% data coverage existed for the overpass and that cloud cover in the scene was less than 5%. This resulted in a total of 255 scenes being pulled for examination of vegetation recovery post-burn scar.

Finally, the VIIRS FEDS daily estimated fire perimeter was obtained from 5 November 2018 to 25 November 2018 to investigate the temporal evolution of the fire's progression. The analysis of perimeter expansion from this dataset reveals the areas most heavily impacted by the fire throughout its duration, providing insight into the locations most severely affected within the burn scar.

### **3.2. 3D WRF ARW Methodology**

The 3D WRF was utilized across 15 separate case dates selected before the end of 2018, but after the Camp Fire was 100% contained on November 25<sup>th</sup>, 2018 so that the most immediate temporal effects from the wildfire could be examined. The case dates were selected in order to represent a range of clear, cumulus, and precipitating conditions (Table 3.1). All of the cases were simulated using the 2016 NLCD-derived LULC data and annual average MODIS greenness fraction from October 2017 to October 2018 to obtain a representation of what the atmospheric responses would look like before the Camp Fire occurred. The cases were then simulated again

using the 2019 NLD-derived LULC data and annual average MODIS greenness fraction from December 2018 to December 2019 to obtain the post-fire truth as perceived by the model. Only the major changes in the domain were updated post-fire, so that the entirety of the burn scar was reflected in post-fire analysis yet nearly everything outside of the burn scar remained the pre-fire conditions (Figure 3.2). This was done in order to only isolate changes that occurred as a result of the alterations of LULC from the Camp Fire. Additionally, this approach removed other factors within the domain that do not have direct impacts on burn scar-forced changes, such as annual snow pack differences in the Sierra Nevada Mountains.

Hourly High-Resolution Rapid Refresh (HRRR) analysis files were input as the boundary conditions for each case date, and each simulation began at 12 UTC on the selected case and was integrated for 36 hours in order to capture the changes in the energy balance across an entire 24-hour diurnal cycle.

Three static domains nested at 9-, 3-, and 1-kilometer grid

spacing were used, with the domains all centered on the city of Paradise, California, located at 39.7558, -121.6198 in the center of the Camp Fire burn scar. Further, the simulations were run

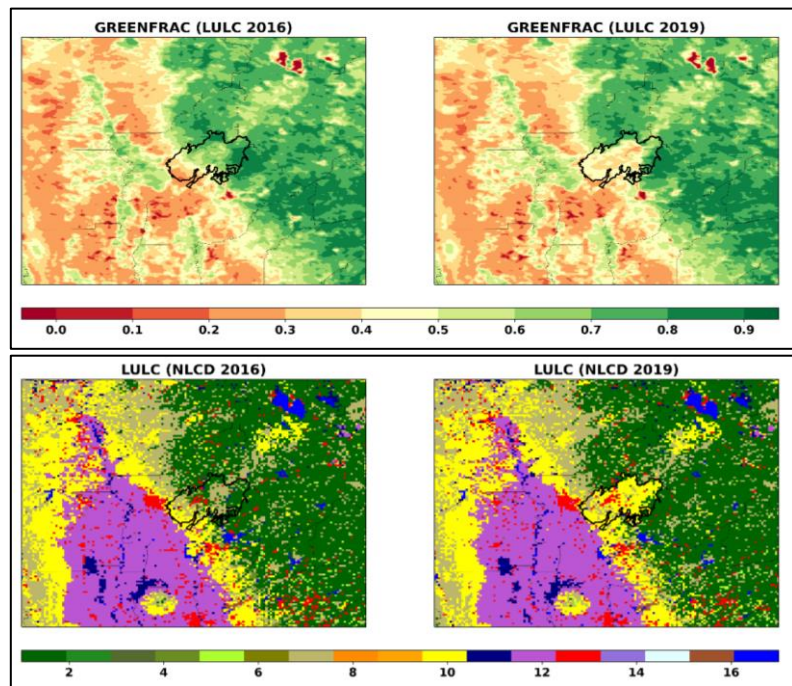


**Figure 3.2:** Green fraction and NLCD classification maps for the innermost WRF domain (D3, see Figure 3.3). The left column is the pre-fire conditions, and the right column is the post-fire conditions as set in the WRF geography files.

with 50 vertical levels, enhancing its ability to represent atmospheric phenomena with greater precision along the vertical axis.

**Table 3.1:** Selected case dates simulated using the 3D WRF ARW. General conditions were determined from visually inspecting MODIS Terra and Aqua visible satellite imagery via the NASA Worldview platform.

Date	Conditions
2018-11-25	Clear
2018-11-30	Cumulus, Precipitation
2018-12-02	Cumulus
2018-12-07	Cumulus
2018-12-10	Cumulus
2018-12-11	Fog to Clear
2018-12-12	Clear
2018-12-13	Clear
2018-12-17	Cumulus, Precipitation
2018-12-25	Clear
2018-12-27	Cumulus to Clear
2018-12-28	Clear
2018-12-29	Clear
2018-12-30	Clear
2018-12-31	Clear

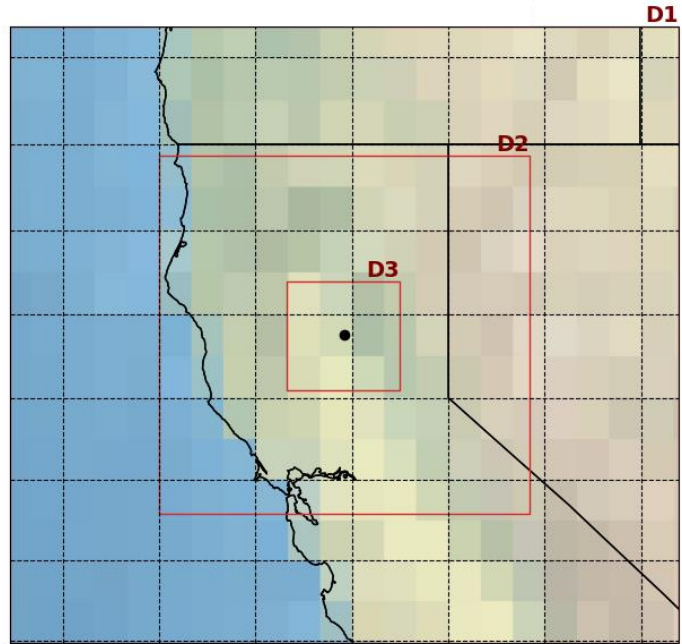


**Figure 3.3:** Study domain of the 3D WRF ARW simulations. The Camp Fire burn scar is located at the center of the innermost domain (D3).

Prior to producing the 30 total model simulations used in this study, sensitivity analysis of physics parameterizations was performed on the WRF-ARW. The PBL and cumulus (CU) parameterizations were altered a total of 9 times for both the pre- and post-fire simulations, using combinations of the PBL 6 (Mellor-Yamada Nakanishi and Niino Level 3 (MYNN3)) (Janjic 1994; Nakanishi and Niino 2006), 1 (Yonsei University (YSU)) (Hong *et al.* 2006), and 16 (E- $\epsilon$  (EEPS)) (Langland and Liou 1996; Zhang *et al.* 2020) and CU 2 (Betts-Miller-Janjic (BMJ)) (Janjic 1994), 3 (Grell-Freitas (GF)) (Grell and Freitas 2014), and 10 (Kain-Fritsch (KF)) (Kain 2004; Berg *et al.* 2013) schemes as inputs. The PBL scheme was chosen to be examined due to the majority of expected alterations to land-atmosphere interactions as a result of the burn scar being located within the PBL as well as to the surface directly. The CU scheme was chosen to be

examined in tandem with the PBL schemes due to some of the selected case dates (Table 3.1) having strong synoptic forcing associated with them, especially the precipitating case dates.

The second domain (D2, Figure 3.3) was used to compare to truth data taken from the Oakland, California upper-air launch site (KOAK) as well as surface data at Chico, CA (KCIC). KOAK was selected due to its being the closest location to the burn scar footprint that allowed for testing of sensitivity through the atmospheric column, and KCIC was chosen for surface sensitivity testing due to it being the closest Automated Surface Observing System (ASOS) location to the burn scar (just outside the western perimeter). The sensitivity analysis was performed at KOAK only for the 2016 LULC simulations as there was no change in the classification at or near that location, but both the 2016 and 2019 LULC simulations were used in the sensitivity analysis for KCIC due to its direct proximity to the burn scar and thus noteworthy LULC change.

After simulating one case date where conditions were majority clear skies (2018 December 30) using each of the 9 possible combinations of the PBL and CU physics parameterizations, the root mean square error (RMSE), mean bias error (MBE), and maximum error (ME) were calculated for the temperature (T), pressure (P), relative humidity (RH), wind speed (WSPD), and wind direction (WDIR) throughout the atmospheric column as well as at the surface (Table 3.2). The combination of PBL scheme 6 (MYNN3) and CU scheme 3 (GF) was selected as the best-fit parameterization combination to use for all 15 cases after reviewing the results of the RMSE, MBE, and ME for both the pre- and post-fire LULC simulations. This parameterization combination showed strong performance in post-fire surface measurements and remained within acceptable ranges at KOAK, making it a reliable proxy for the boundary conditions observed at the burn scar.

**Table 3.2:** Sensitivity analysis results for KOAK and KCIC. The values are reported as RMSE / MBE / ME.

PBL	CU	T	P	RH	WSPD	WDIR
UNITS:		K	hPa	%	m s <sup>-1</sup>	Degrees (°)
<b>KOAK (2016 LULC; Vertical Profile Measurements)</b>						
6	10	1.25 / -0.36 / 4.53	0.98 / -0.38 / 2.10	15.27 / 4.58 / 19.82	2.07 / -0.71 / 6.34	173.88 / -11.34 / 331.19
6	2	1.25 / -0.35 / 4.53	1.02 / -0.45 / 2.13	14.83 / 3.70 / 20.57	2.11 / -0.75 / 6.44	177.66 / -19.35 / 331.79
6	3	1.25 / -0.37 / 4.49	0.98 / -0.36 / 2.13	14.86 / 4.68 / 19.81	2.01 / -0.66 / 6.22	174.70 / -10.69 / 331.14
1	10	1.28 / -0.31 / 4.53	0.92 / -0.36 / 1.92	13.65 / 3.94 / 21.86	1.72 / -0.37 / 5.71	165.76 / -8.46 / 348.15
1	2	1.30 / -0.32 / 4.53	0.96 / -0.42 / 2.10	14.68 / 2.88 / 22.11	1.79 / -0.41 / 5.95	171.15 / -15.22 / 347.43
1	3	1.27 / -0.34 / 4.51	0.91 / -0.32 / 1.96	13.13 / 3.81 / 21.88	1.64 / -0.26 / 5.39	158.35 / 2.54 / 348.68
16	10	1.34 / -0.25 / 4.53	1.07 / -0.56 / 2.20	12.25 / 2.78 / 22.27	1.75 / -0.26 / 5.61	176.02 / -17.24 / 347.64
16	2	1.35 / -0.25 / 4.54	1.09 / -0.61 / 2.08	13.06 / 2.16 / 22.27	1.77 / -0.38 / 5.62	171.93 / -14.06 / 345.17
16	3	1.34 / -0.27 / 4.51	1.06 / -0.55 / 2.07	12.59 / 3.51 / 22.27	1.75 / -0.28 / 5.62	173.56 / -15.70 / 347.04
<b>KCIC (2016 LULC; Surface Measurements)</b>						
6	10	2.29 / -0.92 / 4.87	0.85 / -0.46 / 1.56	16.72 / 1.39 / 20.71	1.42 / -0.00 / 2.78	176.67 / 2.78 / 288.22
6	2	2.33 / -0.97 / 5.00	0.91 / -0.51 / 1.64	16.60 / -0.03 / 19.41	1.47 / -0.03 / 3.27	177.21 / 3.27 / 283.38
6	3	2.27 / -0.92 / 4.91	0.86 / -0.46 / 1.53	16.91 / -0.01 / 20.50	1.47 / -0.01 / 2.86	167.31 / 2.86 / 288.49
1	10	1.91 / 0.23 / 3.47	0.89 / -0.55 / 1.69	17.69 / -7.64 / 33.02	1.42 / 0.65 / 1.05	171.98 / 1.05 / 314.91
1	2	1.92 / 0.32 / 3.38	0.98 / -0.62 / 1.99	18.95 / 0.65 / 40.30	1.39 / 0.65 / 1.08	174.12 / 1.08 / 295.85
1	3	1.90 / 0.26 / 3.37	0.89 / -0.53 / 1.63	17.83 / 0.64 / 34.27	1.44 / 0.64 / 1.00	169.26 / 1.00 / 315.99
16	10	2.06 / 0.61 / 3.31	0.98 / -0.63 / 2.08	20.45 / 0.58 / 40.59	1.32 / 0.58 / 1.36	191.63 / 1.36 / 312.17
16	2	2.03 / 0.54 / 3.33	1.05 / -0.69 / 2.22	21.08 / 0.60 / 43.95	1.34 / 0.60 / 1.02	212.56 / 1.02 / 341.97
16	3	1.99 / 0.53 / 3.34	0.98 / -0.63 / 2.05	19.92 / 0.56 / 37.99	1.30 / 0.56 / 1.20	191.86 / 1.20 / 310.44
<b>KCIC (2019 LULC; Surface Measurements)</b>						
6	10	1.99 / -0.58 / 3.99	0.88 / -0.50 / 1.62	15.44 / -0.80 / 22.66	1.46 / -0.09 / 2.86	187.05 / 2.86 / 325.41
6	2	1.95 / -0.61 / 4.07	0.95 / -0.56 / 1.75	15.08 / -0.04 / 20.61	1.46 / -0.04 / 2.96	195.68 / 2.96 / 325.66
6	3	1.93 / -0.64 / 4.02	0.86 / -0.48 / 1.57	15.44 / -0.19 / 23.45	1.45 / -0.09 / 2.82	186.98 / 2.82 / 323.14
1	10	1.79 / 0.42 / 2.88	0.89 / -0.56 / 1.69	17.09 / -9.01 / 32.21	1.55 / 0.62 / 1.10	172.51 / 1.10 / 315.82
1	2	1.87 / 0.56 / 2.75	1.00 / -0.65 / 2.09	19.57 / 0.70 / 45.66	1.47 / 0.70 / 1.30	175.47 / 1.30 / 302.85
1	3	1.81 / 0.45 / 2.91	0.89 / -0.57 / 1.71	17.78 / -9.22 / 35.74	1.50 / 0.64 / 1.15	174.19 / 1.15 / 318.99
16	10	1.99 / 0.82 / 2.59	1.01 / -0.67 / 2.11	20.18 / -12.12 / 39.26	1.29 / 0.59 / 1.07	214.08 / 1.07 / 343.58
16	2	1.91 / 0.74 / 2.77	1.05 / -0.72 / 2.25	20.15 / -12.09 / 40.70	1.35 / 0.58 / 1.24	212.55 / 1.24 / 337.44
16	3	1.98 / 0.79 / 2.72	0.98 / -0.64 / 2.01	19.94 / -11.88 / 37.82	1.26 / 0.52 / 1.06	189.71 / 1.06 / 313.14

## **Chapter 4. Results and Discussion**

The results of the study and their implications are laid out in the following subsections. Section 4.1 will discuss the results of the satellite remote sensing analysis, and Section 4.2 will discuss the results of the WRF simulations over the Camp Fire domain.

### **4.1. Satellite Remote Sensing Results**

MODIS, VIIRS, and HLS satellite remote sensing datasets were all used to examine how land surface properties and local hydrology has been modified due to drastic LULC changes resulting from the 2018 Camp Fire. In analyzing the four selected MODIS-derived variables of LST Day, LST Night, NDVI, and WSA albedo, significant changes were observed after the Camp Fire was contained. The most drastic changes were noted in the Day LST and NDVI values, where the mean LST Day difference was an increase of 2.5 K and the mean NDVI difference was a decrease of 0.12 across the extent of the burn scar. The Night LST difference was less drastic, but still substantial, with a mean difference of -0.35 K. The mean WSA albedo difference was an increase of merely 0.01, but there was more variability noted in the spatial difference map (Figure 3d), where the hottest portions of the fire saw a larger net increase in WSA albedo while the cooler areas of the fire near the perimeter saw no change to a slight decrease.

**Table 4.1:** Mean, Maximum, and Minimum values of MODIS-derived variables examined pre-fire, post-fire, and the difference between post- and pre-fire, subset to the extent of the burn scar. Note that there was no decrease in the Day LST across the entire extent of the burn scar, thus a maximum decrease of +0.47 K indicates that the entire burn scar footprint experienced an increase of at least 0.47 K post- minus pre-fire.

<b>MODIS PRODUCT:</b>	<b>LST Day (K)</b>	<b>LST Night (K)</b>	<b>NDVI</b>	<b>WSA Albedo</b>
<b>2015-2018 Maximum</b>	308.33	286.20	0.86	0.20
<b>2015-2018 Mean</b>	298.63	284.01	0.63	0.12
<b>2015-2018 Minimum</b>	288.89	280.71	0.21	0.07
<b>2019-2022 Maximum</b>	309.28	286.20	0.81	0.19
<b>2015-2022 Mean</b>	301.14	283.66	0.52	0.12
<b>2015-2022 Minimum</b>	290.54	280.63	0.21	0.07
<b>Maximum Increase</b>	6.12	0.64	0.01	0.06
<b>Mean Difference</b>	2.50	-0.35	-0.12	0.01
<b>Maximum Decrease</b>	+ 0.47	-1.56	-0.41	-0.04

It should be noted that all of the maximum differences of Day LST, Night LST, NDVI, and WSA albedo were seen where the mean FRP was the highest. FRP is the rate of emission of the fire’s radiative energy, and was detected by MODIS overpasses when the Camp Fire was active. Thus, consistently high FRP over the same region within the Camp Fire burn scar extent indicates that those areas were most impacted by the hottest portion of the fire. Day LST increases post-fire of up to 6.1 K were seen where the FRP was at its highest. This massive temperature increase post-fire can be connected to the removal of the majority - if not all of - the vegetative cover in the north-central and central portions of the Camp Fire extent, leading to an increase in albedo and reduction of emissivity. This response is further reflected in reduced transpiration and evapotranspiration across the impacted area. This in turn leads to a decreased cooling effect and lower heat capacity. This relationship would prompt a decrease in NDVI and Night LST as well, due to the removal of healthy vegetation increasing the rate of nighttime radiative cooling (thereby increasing the diurnal temperature range (DTR)), which is what is seen in Figure 4.

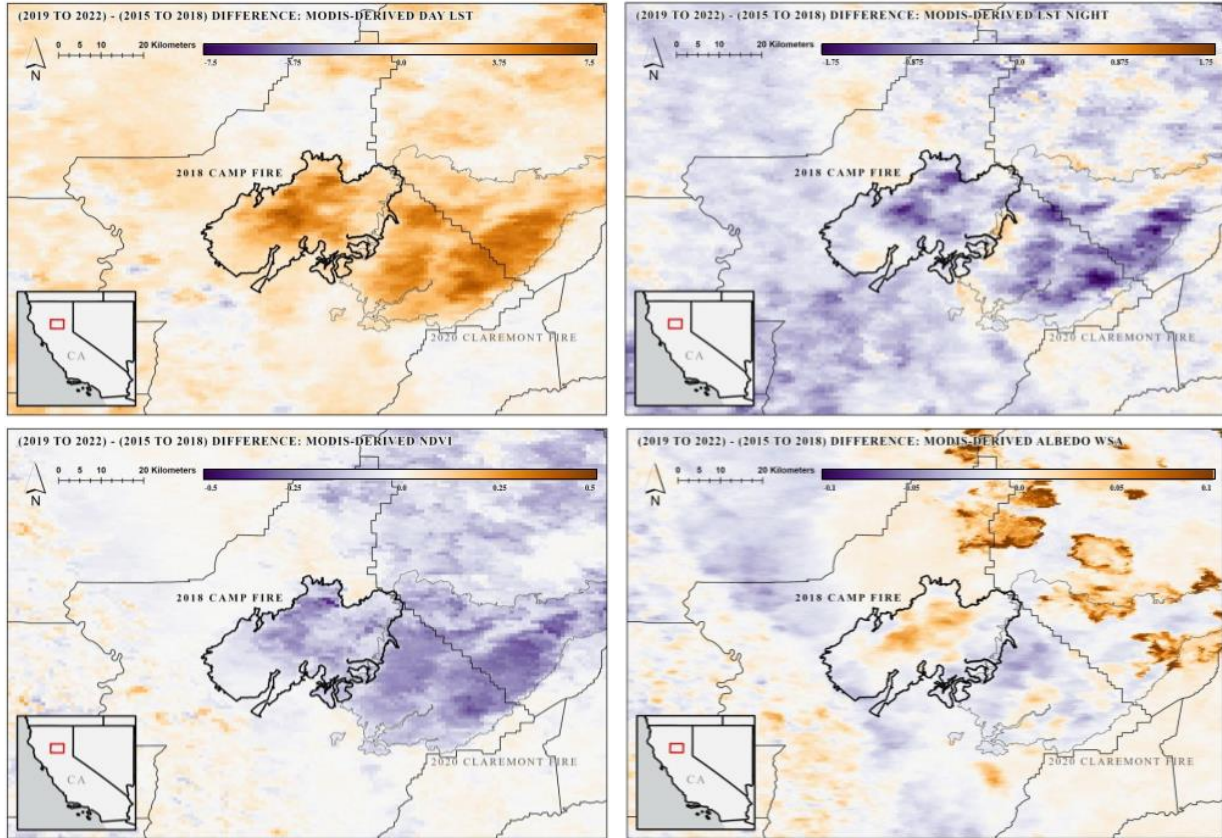


**Figure 4.1:** Pre-fire subtracted from post-fire three-year monthly mean differences of a) LST Day, b) LST Night, c) NDVI, and d) Albedo WSA over the Camp Fire burn scar domain. The thick black outline is the perimeter of the Camp Fire burn scar. The light grey outline to the southeast of the 2018 Camp Fire burn scar is the perimeter of the 2020 Claremont Fire burn scar, which exhibited similar responses of land-atmosphere interactions. The splotches most noticeable in the northeast portion of the Albedo WSA difference map are due to changes in the observed snowpack of the Sierra Nevada Mountains between the 3-year time periods utilized.

It deserves attention that the 2020 Claremont Fire occurred directly to the east of the 2018 Camp Fire, and its impacts on the four MODIS variables examined is also quite prevalent (Figure 4.1). The mean LST Day, LST Night, NDVI, and Albedo WSA differences within the Claremont Fire burn scar extent were +2.88 K, -0.42 K, -0.19, and -0.0008, respectively. These results are consistent with the results obtained from the Camp Fire burn scar extent, with the exception of Albedo WSA differences. This is likely due to the Camp Fire being a much hotter fire (in terms of FRP) than the Claremont Fire despite burn severity estimates via the MTBS

database being higher within the Claremont Fire burn scar extent. This indicates that surfaces within the Camp Fire burn scar extent were more completely charred than within the Claremont Fire, but the Claremont Fire was more impactful on the vegetation cover.

Seasonal Mann-Kendall and Theil-Sen Slope analyses were conducted on each of the four MODIS variables to discern the perceived rate of change attributable directly to the wildfire, rather than any ongoing background climatological alterations. This analysis was performed on the subset of the data over the Camp Fire burn scar extent. Hence, Thiel-Sen slopes were computed over a 20-year period from 2002-2022 and broken into pre-fire and post-fire years (2002-2017 and 2018-2022). This 20-year period of data was spatially averaged across the entire burn scar footprint and temporally averaged by month. Figure 4.2 shows the pre- and post-fire Sen slope analysis alongside the observed data as well as the seasonally decomposed trend for each of the four variables in question.

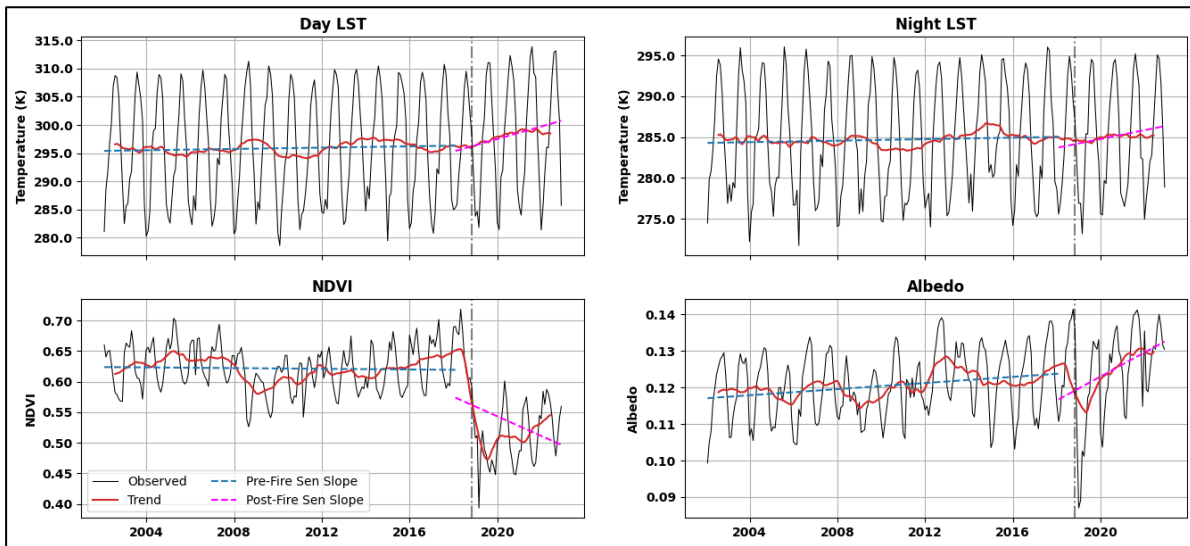


**Figure 4.2:** Monthly mean spatially-averaged time series across the Camp Fire burn scar extent for Day LST, Night LST, NDVI, and Albedo WSA (black lines). The Theil-Sen slopes were computed pre- versus post-wildfire (blue and magenta dashed lines), and the observed seasonally decomposed trend of the data is displayed as the thick red line in each subplot. The fire was active at the vertical dashed line.

The NDVI data exhibited the most significantly pronounced shift in Sen slopes after the 2018 Camp Fire compared to the preceding period. NDVI across the burn scar extent experienced two orders of magnitude increase in negative Sen slope, with the pre-fire Sen slope of  $-7.76e-7 \text{ month}^{-1}$  and a post-fire Sen slope of  $-4.40e-5 \text{ month}^{-1}$ . LST Day also experienced a noticeable increase in its Sen slope, from  $1.59e-4 \text{ K month}^{-1}$  pre-fire to  $3.04e-3 \text{ K month}^{-1}$  post-fire. LST Night also experienced an increase in its Sen slope from  $1.25e-4 \text{ K month}^{-1}$  to  $1.48e-3 \text{ K month}^{-1}$  despite the spatially mapped difference showing a mean decrease in LST Night values (Figure 3.3). The magnitude of the Sen slope has increased despite a mean LST Night decrease due to the ecosystem within the burn scar extent slowly recovering vegetation cover to pre-fire levels. The response seen in albedo was also quite notable, with a sharp drop noted directly after the Camp Fire, but a rapid ascent back to near pre-fire levels shortly thereafter, with an impressive post-fire Sen slope of  $8.98e-6 \text{ month}^{-1}$  ( $p < 0.10$ ) compared to the pre-fire Sen slope of  $1.15e-6 \text{ month}^{-1}$  ( $p < 0.05$ ). Table 4.2 displays the results of the Theil-Sen and Mann-Kendall analyses performed on the MODIS time series data.

**Table 4.2:** Pre-and post-fire statistical analysis of MODIS-derived variables examined over the Camp Fire burn scar extent from 2002-2022. Pre-fire years are 2002-2017, while post-fire years are 2018-2022.

MODIS PRODUCT	Pre-Fire Sen Slope	Pre-Fire P-Value	Post-Fire Sen Slope	Post-Fire P-Value
LST Day	$1.587e-4$	0.576	$3.045e-3$	0.226
LST Night	$1.251e-4$	0.662	$1.481e-3$	0.363
NDVI	$-7.763e-7$	0.467	$-4.380e-5$	0.106
Albedo WSA	$1.151e-6$	0.003	$8.997e-6$	0.007

Further, analysis of daily VIIRS FEDS fire perimeter mapping revealed that the hottest parts of the fire in terms of mean FRP as well as the most quickly impacted areas in terms of fire progression were located between the towns of Buck's Lake and Paradise, CA in the north-central portion of the burn scar. The first several days of active fire conditions saw a rapid spread

of the wildfire to the west into this area, and the fire was not contained for numerous days. The resultant LULC and greenness fraction changes were the starkest in this same area as a result.

These findings carry profound implications for wildfire management and land-use policies, highlighting the importance of refined considerations in the aftermath of such events. The large observed increase in LST Day within the burn scar post-fire underlines the need for localized assessments of the impacts of post-fire heat stress on recovery efforts. The discrepancy between burn severity and fire intensity, particularly evident in albedo WSA differences, emphasizes the complexity of post-wildfire ecological impacts and challenges the conventional understanding of burn severity as a singular metric. The observed NDVI decreases and the slow rate of recovery raises concerns about long-term vegetation and ecosystem health in impacted regions. As the study provides crucial insights into the temporal dynamics of several MODIS-derived variables pertaining to land surface properties, policymakers and land managers can use this information to tailor strategies for effective wildfire risk mitigation, ecological restoration, and sustainable land-use planning. Incorporating the findings on how land-atmosphere interactions are altered post-fire into land management practices is essential for promoting resilient ecosystems and communities in fire-prone regions.

#### **4.2. 3D WRF ARW Results**

The results obtained from the 30 conducted WRF simulations revealed important relationships between drastic LULC change and localized weather and climate pattern shifts. These results will be laid out in the following subsections below, first focusing on the modeled changes in land surface properties, followed by the modeled changes in the local energy balance. The focus will then shift to the modeled changes in the local boundary layer features, ending on

cloud forcing and precipitation footprints. Note that Table A.1 found in Appendix I will be referenced throughout these results.

#### **4.2.1. Modeled Changes in Land Surface Properties**

The first crucial examination of the WRF simulation results is found in the modeled changes in land surface properties. Diagnosing the differences in greenness fraction, albedo, emissivity, soil moisture, and LST is necessary to understanding the land-atmosphere interactions that may change as a result of the wildfire burn scar. Examining these variables in particular can also allow for easy comparison to comparable MODIS-derived variables, reported in section 4.1. It should be noted that some of the differences between the modeled results and observed MODIS results discussed below can be attributed to the temporal differences in the data. The modeled results only encompass a range of dates of just over one month, directly after the fire was contained. The MODIS observations, in contrast, represent the difference averaged over three years before and after the wildfire occurred.

Spatial difference plots, averaged across all 15 case days for one diurnal cycle (which is defined as the 24-hour period of 13 to 13 UTC for this study), were created to inspect the pattern and magnitude of any changes that occurred post-fire compared to the pre-fire conditions. Domain 3 of the WRF grid was utilized for these plots, as it has the highest spatial and temporal resolution. Greenness fraction (or vegetation fraction), which is the percentage of the grid cell that contains vegetation cover, was first examined to ensure that the changes were representative of what was seen in the MODIS NDVI differences post-fire compared to pre-fire. It was found that the modeled changes in greenness fraction were comparable to what was found in the

MODIS-derived NDVI differences (Table 4.1), with a mean difference of WRF greenness fraction of nearly -10% within the burn scar (Table A.1).

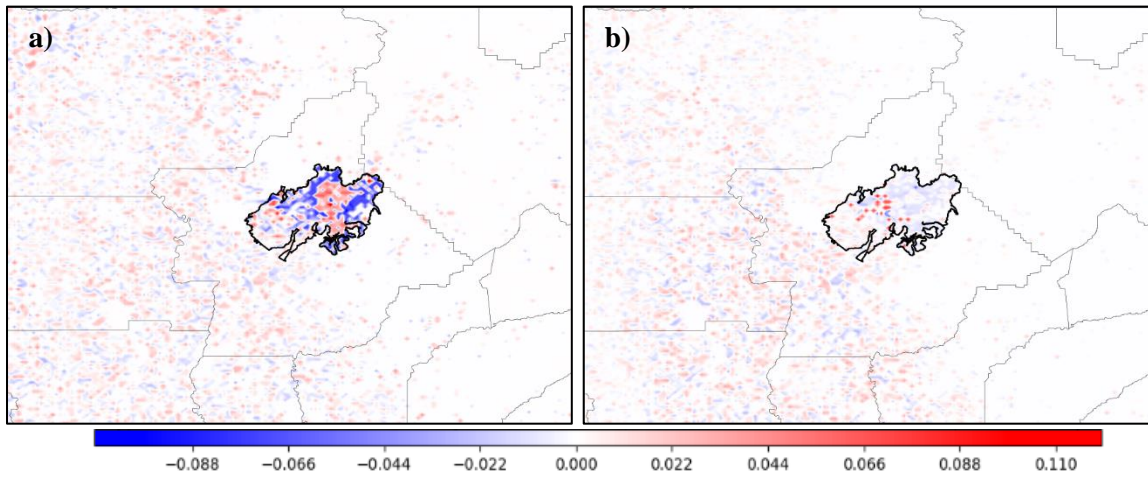


**Figure 4.3:** Run-averaged spatial difference plot of albedo (a) and emissivity (b), averaged across one diurnal cycle, subset to domain 3 of the WRF simulations. The thick black outline is the burn scar perimeter extent.

Once it was confirmed that the WRF output reflected similar changes in greenness fraction to that of MODIS-derived NDVI, the albedo, emissivity, and soil moisture variables were examined. The average difference in albedo as modeled by the WRF simulations, spatially averaged over the burn scar perimeter extent, was just over 0.01 (Table A.1), which once again is comparable to the MODIS-derived Albedo WSA difference spatially averaged over the same area (Table 4.1). The spatial pattern of the difference in average albedo was also found to be analogous to the MODIS-derived results (Figure 4.3). Both the MODIS-derived differences in albedo WSA and the WRF albedo output were shown to be largely positive in the center of the burn scar, while the edges of the burn scar (especially in the east) revealed a decrease in albedo. The biggest increases in albedo in both products is centered around Buck's Lake, CA, located in the Plumas National Forest. This modeled increase overlaps nearly exactly the location of the hottest portion of the Camp Fire in terms of FRP. While a hotter fire would char the area more completely, and a decrease in albedo would thus be expected, the resulting LULC change here

was from predominantly evergreen forest to grassland (Figure 3.1). Thus, what remained of the vegetation post-fire was newly exposed to direct sunlight, and Stull (1988) reveals that grassland LULC typically has higher albedo than evergreen forest. Recall that the post-fire LULC was derived from the end of 2019, which allowed for one year's worth of vegetation regrowth to be accounted for post-fire.

The response in emissivity across the burn scar was as expected based on prior studies, revealing a small decrease across the majority of the burned area. The burn scar average decrease in emissivity was -0.19 % (Table A.1; Figure 4.3). Further the response in soil moisture was also as expected based on prior research, with an average decrease of  $-0.08 \text{ cm}^3 \text{ cm}^{-3}$  across the burn scar through all four modeled soil levels (Table A.1).

After exploring the changes in greenness fraction, albedo, emissivity, and soil moisture output from the WRF simulations and ensuring that they largely match the results reported from the MODIS-derived NDVI and WSA albedo as well as the findings of prior studies, the LST output was examined in three subsets. The LST was first plotted as a spatial difference map in the same manner as the previous WRF output, subset to one 24-hour diurnal cycle from 13 UTC – 13 UTC. Arbitrary LST Day (16-00 UTC) and Night (13-16; 00-13 UTC) temporal ranges were also set from this diurnal cycle and plotted spatially in order to more completely compare the results of the WRF simulations with that of the MODIS-derived variables (Figure 4.4 a, b).

The WRF output LST results largely complemented those seen from the MODIS-derived LST Day and Night products (Table 4.1; Figure 4.1). The average difference in WRF output LST Day within the burn scar perimeter extent was an increase of  $\sim 0.27 \text{ K}$  (Table A.1), while the average difference in LST Night was a decrease of  $\sim -0.27 \text{ K}$  (Table A.1). In other words, the diurnal temperature range (DTR) of the burn scar extent increased post-fire by  $\sim 5\%$ . The spatial

distribution of LST Day difference have a smaller increase footprint than that of the MODIS-derived LST Day due to the western portion of the burn scar extent showing a net decrease in LST post-fire compared to pre-fire (Figure 3.1). This is largely tied back to the temporal differences between the satellite observations and the model simulations. However, the overall consequences of the burn scar remain the same, with a net increase in daytime LST within the extent of the scar and very little to no change outside of the scar. A sub-feature to note from the LST Day and Night WRF output results is that the largest increase in LST Day ( $>9$  K) occurred over the city of Paradise. This contrasts with the MODIS-derived results, which show the largest changes in LST Day over the hottest portion of the fire per FRP, east of Paradise. As a result, the LULC changes were different between Paradise (urban) and the forest to the east, so the observed MODIS changes were lower by  $\sim 2$ - $3$  K (Table 4.1). However, the WRF results did still show large and comparable changes in Day LST over the highest FRP region east of Paradise as well as the largest decrease in LST Night of  $\sim 1$ - $2$  K (Figure 4.5 b).

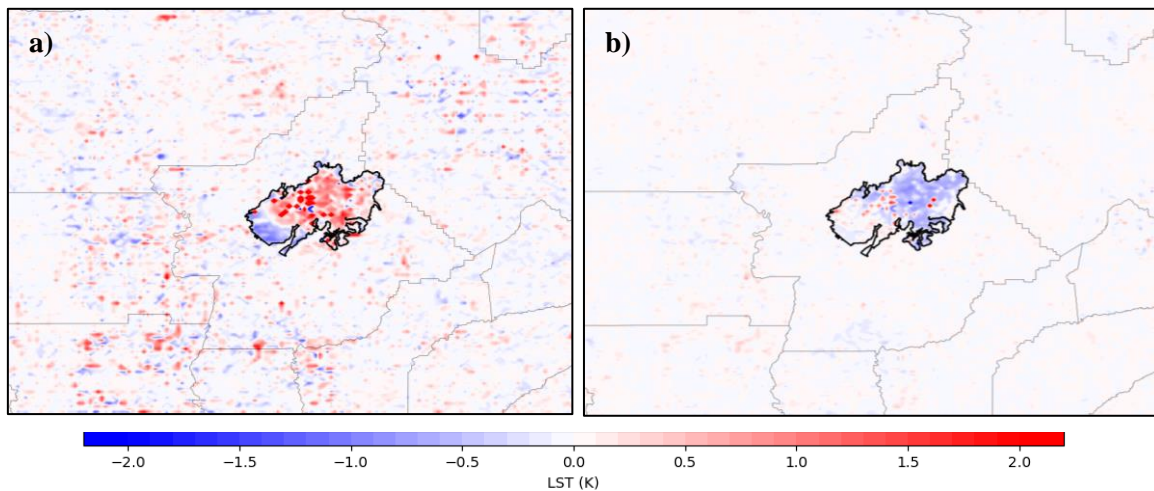


**Figure 4.4:** Run-averaged, spatial difference plots of LST from domain 3 of the WRF output. A LST Day (a) and LST Night (b) spatial difference map is all presented here.

Finally, time series analysis was performed on the LST WRF output. The time series of LST was averaged across all case dates, and plotted across the same pre-defined 24-hour diurnal cycle. This analysis was both spatially averaged across the entire burn scar perimeter extent (Figure 4.5), as well as pulled for coordinate point locations for both the city of Paradise, CA (39.7626, -121.5968) and Buck’s Lake, CA (39.9432, -121.2025). This analysis allowed for more complete understanding of how different LULC changes impacted the modifications to LST throughout the diurnal cycle post-fire compared to pre-fire simulations. When examining the burn scar as a whole, an opposite LST response appears when comparing peak heating to overnight conditions. During peak heating hours ( $\sim 20:30 \pm 2$  UTC), the average across the entire burn scar extent reveals an increase in LST post-fire compared to pre-fire conditions by  $\sim 0.5$  K. This further substantiates the results from spatial analysis of LST, which also shows a net increase in most areas during the daytime (Figure 4.4). However, during the afternoon-evening transition (AET) period within the PBL and into the overnight hours when a nocturnal boundary layer (NBL) would be present, LST post-fire is lower than pre-fire by  $\sim 0.25$  K.

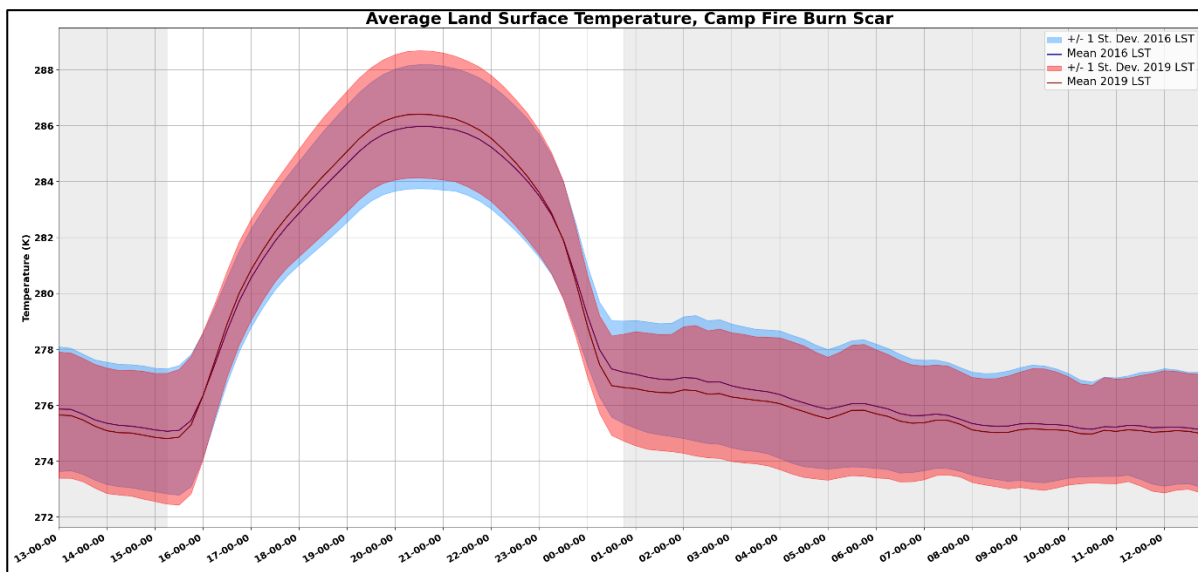


**Figure 4.5:** Time series analysis of WRF output LST for the spatially-averaged burn scar extent. Pre-fire LULC WRF simulation output is plotted in blue, and post-fire is plotted in red on each subplot, with shadings enveloping the range of  $\pm 1$  standard deviation

The Paradise point location was chosen to analyze in more detail, as this location was majority urban LULC pre-fire, but 95% of the city was burnt down from the wildfire. A similar pattern was revealed to that of the burn scar spatial average during peak heating at Paradise, where post-fire LST is higher than pre-fire LST by just under 1 K. There is also a similar pattern to that of the burn scar spatial average when examining the AET into overnight period of the time series, with an even bigger LST difference observed during the AET at this location (~ -1.2 K). This observed variation can be attributed to factors such as differences in soil moisture or cloud forcing (section 4.2.4). The influence of a shallower planetary boundary layer height (PBLH) is also observed during these hours, further amplifying these effects (section 4.2.3).

The location at Buck's Lake, however, shows a substantial increase in LST across the entire day time post-fire compared to pre-fire, with a relatively uniform 2-5 K increase at all time steps and a similar LST Night response as what was seen at the other examined locations. This location, once again, is where the maximum FRP was the highest, indicating the fire burned the hottest here and charred the ground most completely. It also is where the MODIS-derived LST, albedo, and NDVI were most drastically altered by the wildfire (Figure 4.1).

#### **4.2.2. Modeled Changes in the Local Surface Energy Balance**

After examining how the land surface properties were modeled to have changed post-fire compared to pre-fire conditions, the modeled changes in the local surface energy balance must be considered. The energy balance of the Earth can be represented by the simple formula representing shortwave and longwave radiation (Equation 1):

$$\frac{S_0}{4}(1 - \alpha) = \varepsilon\sigma T^4 . \quad (1)$$

In Equation 1,  $S_0$  is the solar constant, equivalent to approximately  $1367 \text{ Wm}^{-2}$ . This constant is divided by four in order to account for the surface area of the Earth receiving solar radiation at any given time. Alpha ( $\alpha$ ) is the planetary albedo, which is the fraction of solar radiation reflected back to space by the Earth. The average planetary albedo is approximately 0.295. Epsilon ( $\epsilon$ ) is the emissivity, which can be equated to 1.0 for a blackbody. Sigma ( $\sigma$ ) is the Stefan-Boltzmann constant, equated to  $5.67 \times 10^{-8} \text{ Wm}^{-2} \text{ K}^{-4}$ . This constant relates the energy radiated by a blackbody to its temperature. Finally,  $T$  in Equation 1 is the temperature of the planet, given in units of Kelvin (K). It is from this relationship that the Earth's average surface temperature of 288 K is derived.

In addition to this simple relationship of the energy balance, latent heat flux (LE) and sensible heat flux (SH) must also be considered. Latent heat is the heat energy absorbed or released during phase changes, while sensible heat is the heat energy exchanged that results in a change in temperature. Latent heating is often associated with processes in the water cycle such as evaporation and condensation, while sensible heat is often associated with a direct transfer of heat between the Earth's surface and the atmosphere. The common form of the equations for LE and SH are provided in Equations 2 and 3:

$$LE = \rho L \cdot E \quad (2)$$

$$SH = \rho c_p \cdot \Delta T \quad (3)$$

In the above equations, rho ( $\rho$ ) is the air density, typically  $1.225 \text{ kg m}^{-3}$  for standard atmospheric conditions.  $L$  is the latent heat for a given process (*i.e.*,  $L_v$  is the latent heat of vaporization,  $L_f$  is the latent heat of fusion, etc.)- these are all given constants that depend on the temperature of a substance.  $E$  is the rate of the ongoing phase change, whether that be condensation, evaporation, or another phase change.  $c_p$  is the air's specific heat at constant

pressure, a constant approximately equal to  $1004 \text{ J kg}^{-1} \text{ K}^{-1}$ . Finally,  $\Delta T$  is the change in temperature between the surface and air.

In examining the run-averaged spatial difference maps of the modeled LE and SH, it is quite evident that there exists an inverse response between the two variables within the burn scar extent (Figure 4.6). There are two main areas of interest revealed in the inspection of LE and SH differences post-fire compared to pre-fire. The first such area is the pre-fire urban LULC of the city of Paradise, where post-fire changes in LE and SH reveal a sharp increase in LE of  $\sim 10 \text{ Wm}^{-2}$  and comparable but not quite as impressive decrease in SH of  $\sim 5 \text{ Wm}^{-2}$  over the same geographic region. The largest driver of this increase in LE and decrease in SH over the Paradise area can be attributed to changes the vegetation canopy following the wildfire. The exposure of lower-lying vegetation that was previously covered by forest can contribute greatly to the observed rise in LE. Concurrently, the reduction in SH can be attributed to the loss of impervious surfaces and changes in thermal properties associated with the altered land cover. However, other factors may be at play here as well, such as changes in the surface roughness of the land from urban to pasture / grasslands (Figure 3.1).

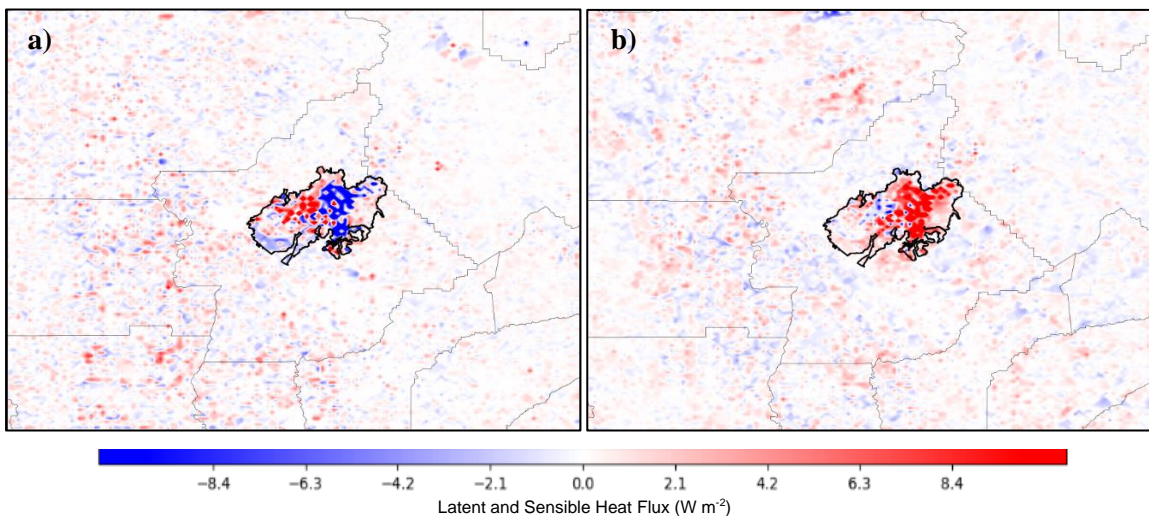


**Figure 4.6:** Run-averaged, spatial difference plots of latent (a) and sensible (b) heat fluxes over WRF domain 3, averaged over a 24-hour diurnal cycle from 13-13 UTC.

The second such area is the eastern portion of the burn scar extent, in the vicinity of Buck's Lake. In this region, a large area of decreasing LE of and comparable increasing SH of  $\sim \pm 10 \text{ Wm}^{-2}$  exists. These results match those reported in previous studies of flux response to burned areas (Molders and Kramm 2007). This opposite result to that of the Paradise region can be at least somewhat attributed to the changes in albedo discussed in section 4.2.1 (Figure 4.3). However, this signal more fully complements that of changes in surface roughness. The once rough evergreen forest LULC was effectively removed by the wildfire, turning this region into predominately grassland, pasture, and barren land (Figure 3.1). The removal of heavy vegetation cover in turn reduces the surface roughness and allows for better mixing of the near-surface air, thus enhancing the transfer of SH from the surface to the atmosphere. Additionally, the reduced evaporation and transpiration would suppress cooling through LE, especially in the most severely damaged portions of the burn scar's ecosystem such as near Buck's Lake. There were also observed increases in the ground storage term of the energy budget that supports this increase in SH and decrease in LE over the eastern portion of the burn scar (Figure 4.9 d).

Overall, the average changes in LE and SH across the burn scar are  $\sim -1.5$  and  $\sim +2.4 \text{ Wm}^{-2}$ , respectively (Table A.1). The magnitude of difference in SH being larger than LE can be linked to changes in the stability of the PBL over the burn scar, which is explored in section 4.2.3. Changes in cloud forcing may have also impacted the differences in LE and SH observed over the burn scar, which are explored in section 4.2.4.

The total net radiation for the pre-defined diurnal cycle was also examined, which is the measure of the net energy balance at Earth's surface over a given time interval. For the 24 -hour time period of interest, the total net radiation can be derived from Equation 1 in the following form:

$$Total R_{net} = \int(Q_{in} - Q_{out})dt, \quad (4)$$

where  $Q_{in}$  is the total incoming shortwave and longwave radiation,  $Q_{out}$  is the total outgoing shortwave and longwave radiation, and  $dt$  is the time period of interest. This quantity is thus measured in units of  $MJ m^{-2}$ . In viewing the radiative differences of the burn scar in this way, it is easier to determine what energy change is most impactful in what parts of the burn scar and by what magnitude.

Figure 4.7 reveals that the average difference in total net radiation for the majority of the burn scar is a decrease, bar the far western portion of the burn scar extent. The spatially averaged difference in total net radiation across the burn scar is  $\sim -0.2 MJ m^{-2}$

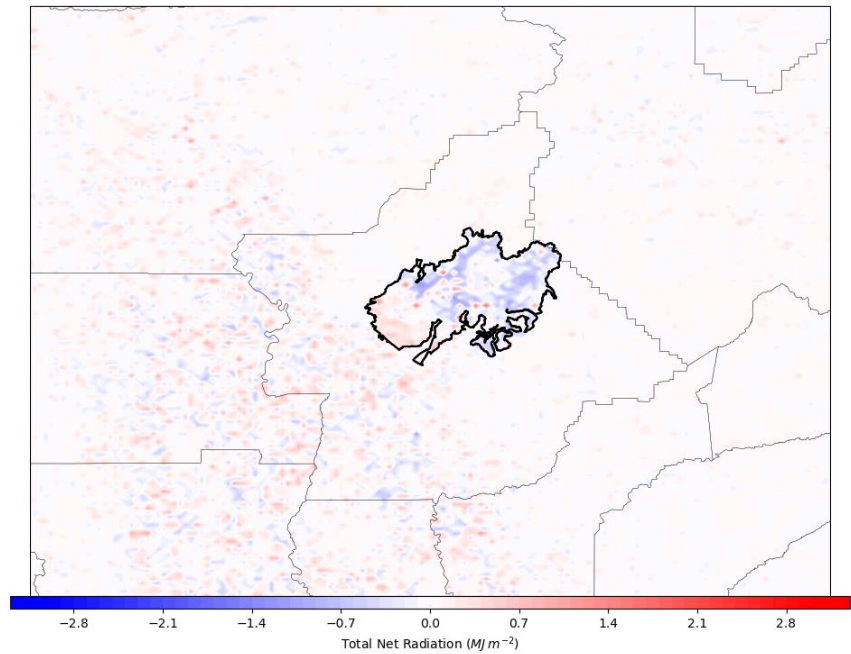


**Figure 4.7:** Run-averaged, spatial difference plots of the total net radiation over WRF domain 3, averaged over a 24-hour diurnal cycle from 13-13 UTC.

expands on this investigation to illustrate how each term of the surface energy budget changes post- compared to pre-fire conditions. This analysis shows that the primary driver of the decrease in total net radiation over the burn scar is related to the increase in upwelling solar radiation, which is the quantification of more sunlight being reflected back to space. This feedback is tied to the overall increase in albedo over the burn scar extent. However, over the hottest observed area of the wildfire, the total net radiation remained at  $\sim 0 MJ m^{-2}$ . This indicates that the fire

burned so hot in this region that the charring of the surface resulted in an even lower albedo than the pre-fire forest LULC (this is supported by Figure 4.3). Thus, the ground was able to absorb more incoming solar radiation, encouraging enough heating of the surface to offset this negative feedback. This result is seen most fully in the MODIS-derived LST Day difference (Figure 4.1 a), but also in the MODIS LST results (Figure 4.4). However, this decreased absorption of shortwave radiation is nearly offset by the longwave radiation emitted from the same geographic region.

It should be noted that the western extent of the burn scar was where the fire was much cooler and LULC was predominantly grassland, so the result was essentially a field fire. Thus, the changes in LULC were not nearly as drastic, but any vegetation that remained post-fire experienced a small increase in albedo

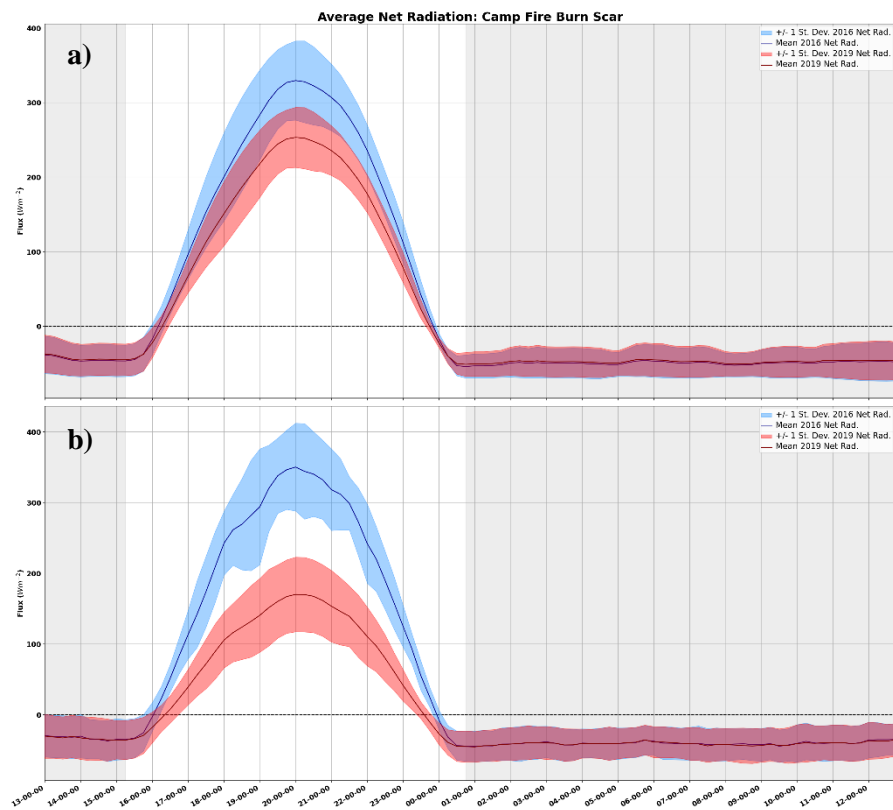


**Figure 4.8:** Time series analysis of WRF output net radiation for a) the spatially-averaged burn scar extent, and b) at Buck's Lake. Pre-fire LULC WRF simulation output is plotted in blue, and post-fire is plotted in red on each subplot. Light grey shading indicates nighttime.

(Figure 4.3) without much difference in surface roughness occurring, which likely is the main forcing for the increase in total net radiation in that area.

Finally, time series analysis of net radiation was performed on the same locations as that of the LST time series analysis in section 4.2.1. These results showed a quite similar pattern to that of the LST time series analysis, which suggests that the change in net radiation as well as LST post-fire compared to pre-fire conditions is the strongest relationship revealed by this study (Figure 4.8; Table 4.1; Table 4.2; Table A.1). The overall net radiation difference across the entire burn scar is nearly negligible if averaged across the entire diurnal cycle, but as was shown in Figures 10 and 11, there is quite marked spatial and temporal variability. The mean burn scar net radiation shows a marked decrease during the daytime hours, with maximum decreases of  $\sim 75 \text{ Wm}^{-2}$  around peak heating (Figure 4.8 a). The point location pulled near Paradise (not shown) displays a similar pattern to the burn scar spatial average time series, with a maximum decrease of  $\sim 50 \text{ Wm}^{-2}$  at peak heating, and a slightly larger increase during the AET compared to the burn scar average. However, when examining the point location at Buck's Lake, much larger signal is unveiled (Figure 4.8 b). The entirety of the daytime hours shows an enormous decrease in net radiation, with the largest decrease around peak heating of  $\sim 175 \text{ Wm}^{-2}$ . As the AET occurs and even extending into the early morning hours, though, there is little to no change in net radiation at Buck's Lake. In contrast, there is a slight increase in nighttime net radiation across the burn scar as a whole as well as at the Paradise location. A large driver of the increase in net radiation during the evening into overnight hours post-fire can be attributed to the lack of any substantial vegetation canopy. The removal of this vegetation allows for more radiation to emit outwards into the atmosphere than it could during pre-fire conditions. The largest driver of the decrease in net radiation throughout the daytime hours can be attributed once again to the increase in upwelling shortwave radiation, though the smaller changes in the other terms that go into net radiation are also at play (Figure 4.9).

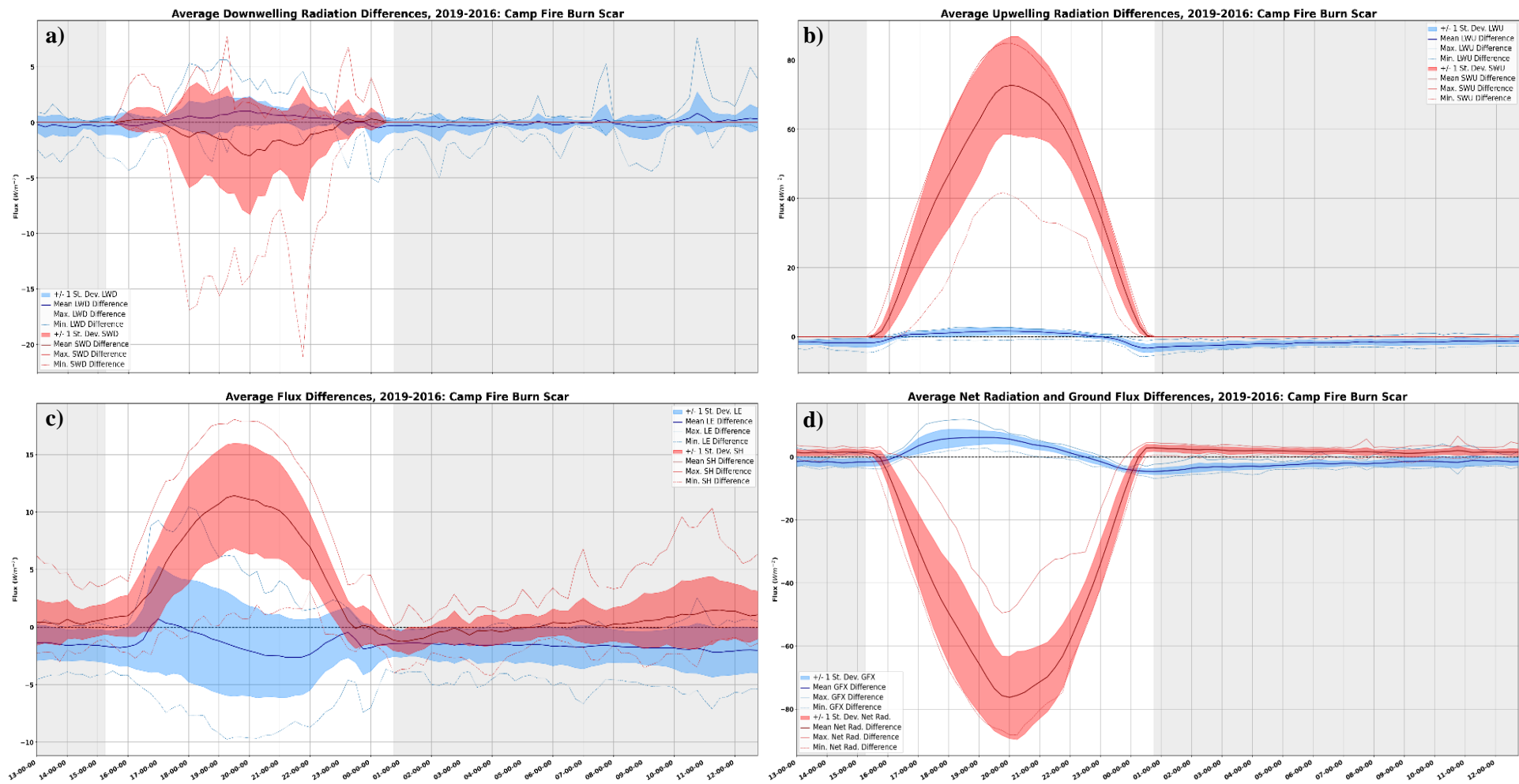


**Figure 4.9:** Burn scar-averaged difference meteograms of the local surface energy budget. Downwelling shortwave and longwave (a), upwelling shortwave and longwave (b), latent and sensible heat fluxes (c), and ground flux and net radiation (d) are all shown. Red and blue shadings are  $\pm 1$  standard deviation from their respective means, and the light grey shadings on each subplot indicate nighttime.

### **4.2.3. Modeled Changes in Local Boundary Layer Features**

After establishing what changes occurred to the land surface and the local energy balance, the modeled changes in local boundary layer features must be considered. Results of modeled temperature and moisture (section 4.2.3.1), as well as the changes to the planetary boundary layer height (PBLH), lifted condensation level (LCL), and level of free convection (LFC) (section 4.2.3.2) will be discussed in this section. Additionally, alterations to wind speed and direction and the impacts on mesoscale circulations (section 4.2.3.3) were examined.

#### **4.2.3.1. Temperature and Moisture**

The temperature and moisture responses within the PBL will first be examined in tandem. Figure 4.10 displays the maximum, minimum, and mean 2-meter temperature, as well as the maximum and minimum differences, averaged across all 15 case days and temporally averaged across the pre-defined 24-hour diurnal cycle. While there was an overall increase in 2-meter temperature across the vast majority of the burn scar extent, the spatial average increase was only  $\sim 0.12$  K due to the enlarged DTR both increasing daytime temperatures and decreasing nighttime temperatures (Table 4.1.1.A). The region at and around Paradise saw the highest modeled decrease in 2-meter temperatures of up to  $\sim 1.5$  K during the nighttime, while there was a relatively uniform increase in daytime 2-meter temperatures across the burn scar of  $\sim 0.25$ - $0.5$  K. Overall, the burn scar spatial average modifications to the 2-meter temperature were  $\sim 0.22$  K at day and  $\sim -0.28$  K at night (Table A.1). Further, in examining the burn scar-averaged time series of temperature (Figure 4.10 f), it becomes apparent that the largest changes in 2-meter temperature occur as the NBL forms at the tail end of the AET, with average decreases in

temperature of  $\sim 0.4$  K. This reduction in nighttime temperature post-fire modifies somewhat throughout the remainder of the night, but still exhibits a net decrease of  $\sim 0.25$  K.

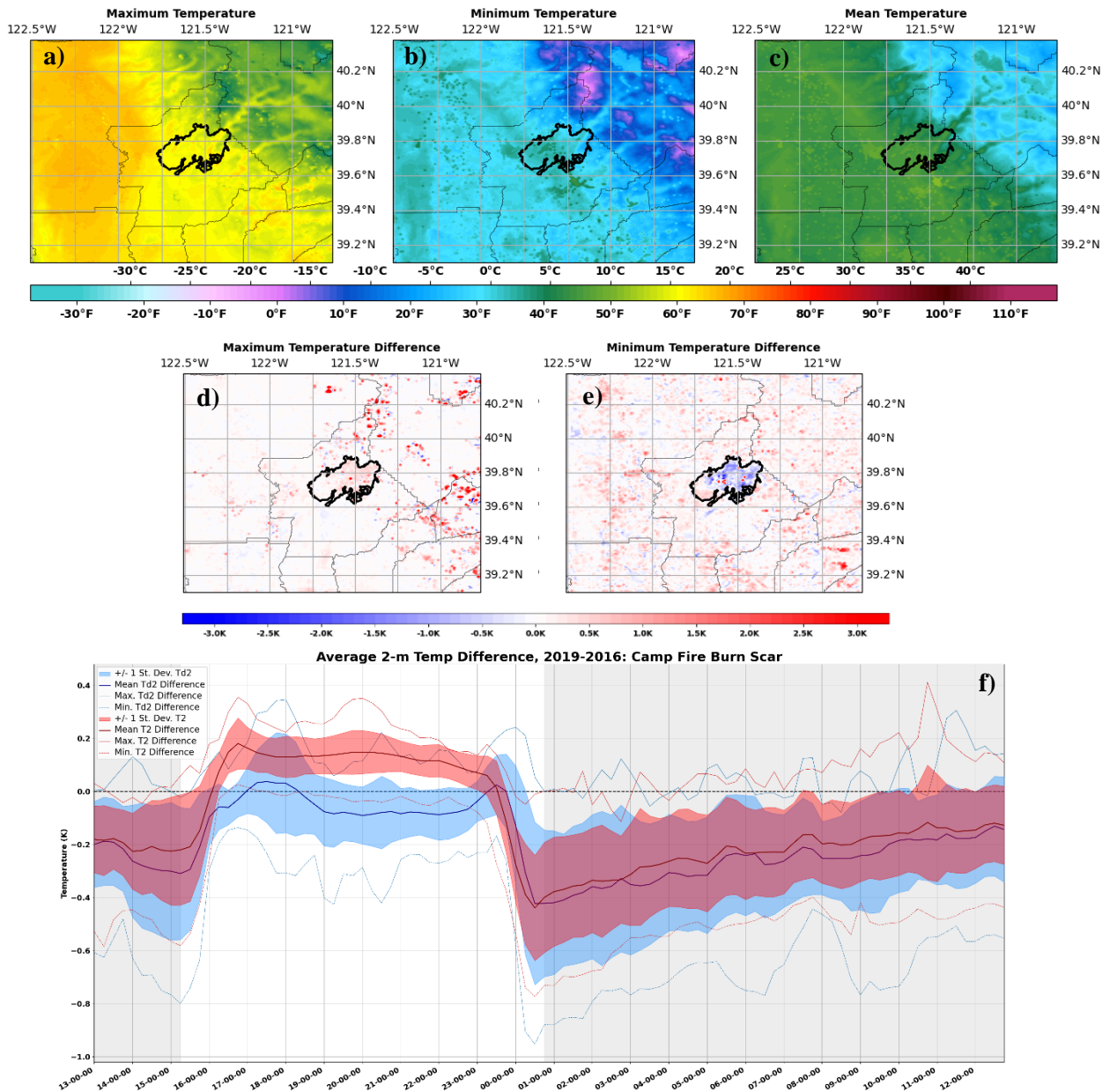


**Figure 4.10:** Maximum (a), minimum (b), and mean (c) 2-meter temperature across domain 3 of the WRF output for all case days, as well as the maximum (d) and minimum (e) temperature differences post-fire compared to pre-fire conditions. Subplot (f) shows the time series analysis of 2-meter temperature (red) and dewpoint (blue) differences post- compared to pre-fire conditions.

The 2-meter dewpoint temperature (Equation 7) was also examined in the same manner as that of 2-meter temperature (Figure 4.10 f; Table A.1). The overall response of the 2-meter

dewpoint temperature was a drying effect across the burn scar. Time series analysis reveals this drying to be amplified during the AET, reaching a mean decrease of  $\sim 0.4$  K and following the same pattern as 2-meter temperature. When examining the daytime hours, though, the combination of increased 2-meter temperature ( $\sim 0.15$  K) and decreased dewpoint temperature ( $\sim -0.1$  K) should have the strongest impact on PBLH and LCL height. First, however, the vertical profile of the PBL must be examined in this same manner with respect to temperature and moisture.

In this examination of the vertical profile of the PBL through time with respect to relative humidity, which is the measure of water vapor present in the air compared to the maximum amount the air could hold at that temperature (Equation 9), the majority of the profile reveals a decrease in moisture content over the burn scar at all locations examined. The following equations derive how to compute dewpoint temperature and relative humidity, using the expressions presented in Bolton (1980). In the below equations,  $e_s$  is the saturation vapor pressure in mB,  $e$  is the vapor pressure in mB, RH is relative humidity in percent, and  $T_d$  is the dewpoint temperature in degrees Celsius ( $^{\circ}\text{C}$ ):

$$e_s = 6.112 \cdot e^{\frac{17.67 \cdot T}{T+243.5}} \quad (5)$$

$$e = 6.112 \cdot e^{\frac{17.67 \cdot T_d}{T_d+243.5}} \quad (6)$$

$$T_d = \frac{\log_{6.112} \frac{e}{e_s} \cdot 243.5}{17.67 - \log_{6.112} \frac{e}{e_s}} \quad (7)$$

$$RH = \frac{e}{e_s} \cdot 100 . \quad (8)$$

Time-height plots for the Paradise point location effectively demonstrate the response to drastic LULC change and unveil the interaction among temperature, moisture, and PBLH

between post- and pre-fire conditions. The run-averaged time-height plot of relative humidity for post-fire conditions at Paradise shows a slight temporal lag between the peak growth of the PBLH and the maximum RH (Figure 4.11 a). This is likely due to the delay in vegetation response to peak heating (Valladares and Pearcy 1997). Additionally, the time-height temperature difference (Figure 4.11 b) confirms that the largest temperature changes are within the surface layer of the PBL, further solidifying the strong relationship between wildfire-driven LULC changes and statistically significant ( $p < 0.05$ ) changes in near-surface temperature (Table A.1). The deeper region of temperature change  $\pm 1$  standard deviation occurring during the daytime compared to the nighttime hours indicates that post-fire conditions are more favorable for stronger boundary layer thermal updrafts, which supports prior research (Hernandez *et al.* 2015; Page 2007; Souza *et al.* 2000) and was also noted in this study particularly over the east half of the burn scar.

Finally, time-height differences in RH were examined at several locations across the burn scar (Paradise shown, Figure 4.11 c). These results confirm that the majority of the atmospheric column located within the PBL and even into the free atmosphere (FA) experiences net drying. The temporal period previously defined as daytime hours (16-00 UTC) shows the most substantial drying in the vertical, which is in contrast to the 2-meter dewpoint decreases being maximized at the end of the AET. Some of this can be explained by drier air mixing down towards the surface layer of the PBL in both pre- and post-fire simulations throughout the AET period, though the post-fire mixing is drier overall. It should be noted that the majority of the PBL experiences decreases in moisture with values less than 1 standard deviation from the mean.

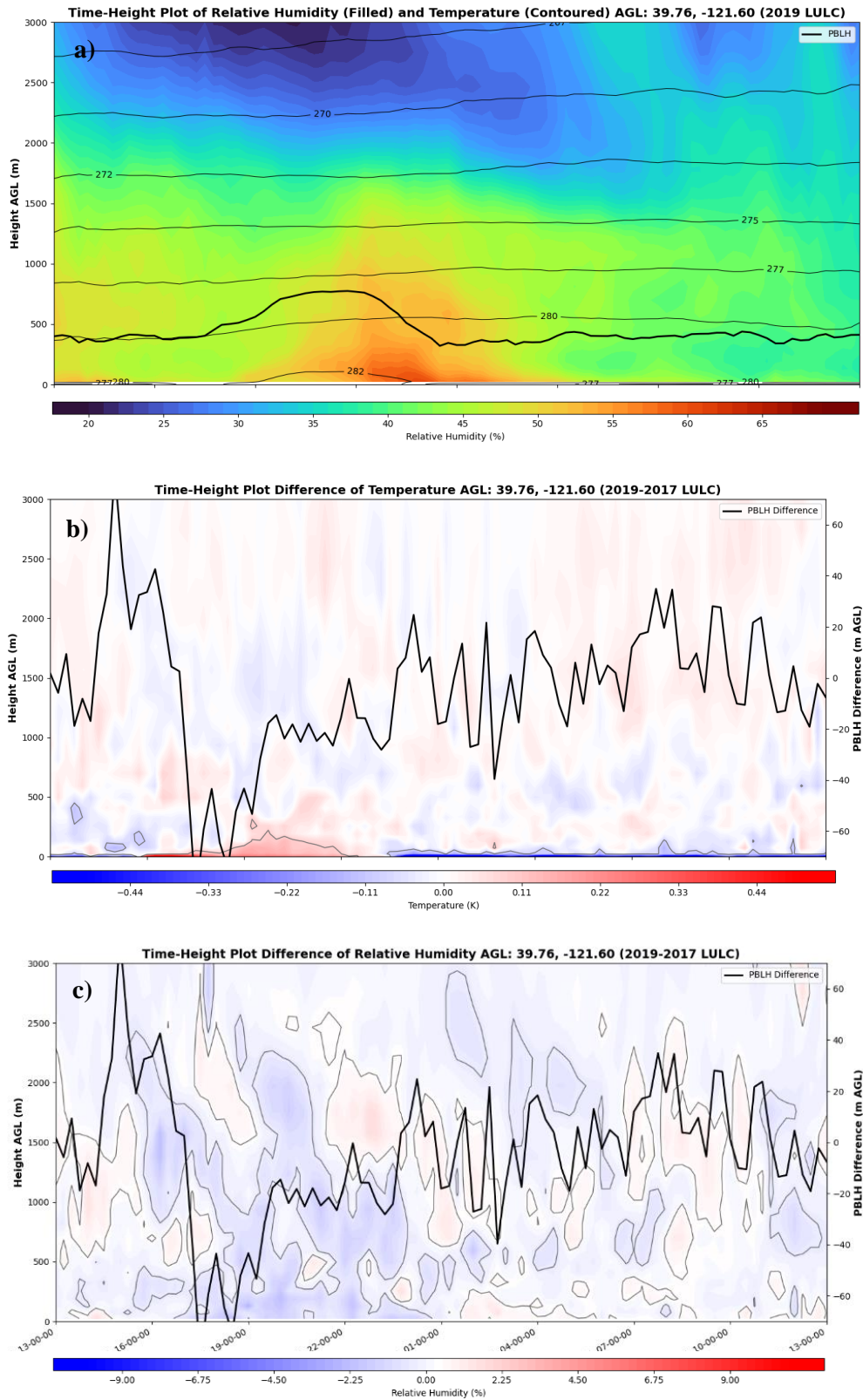


**Figure 4.11:** 24-hour time-height plots illustrating the interaction between temperature, moisture, and the PBLH. Thick black lines are PBLH, and grey lines in b and c are areas where the standard deviation is  $\pm 1.0$ .

#### 4.2.3.2. PBLH, LCL, and LFC

To further illustrate the relationship in the LULC change and temperature and moisture, as well as building a precedent for localized wind shifts discussed later, the PBLH, LCL, LFC, and LCL deficit differences were all examined. While PBLH was pulled directly from the WRF output files, the wrf-python (NCAR Computational and Information Systems Laboratory 2021) and MetPy (May *et al.* 2022) packages were utilized to obtain the LCL and LFC heights. These packages utilize an iterative approach to solve for the LCL and LFC heights in a manner similar to Normand's Rule, which is based on the assumption that the environmental lapse rate ( $\Gamma_{env}$ ) is constant to the point of the LCL and LFC (Equations 9, 10). The only difference in these equations is that LCL utilizes the dry adiabatic lapse rate (DALR;  $\Gamma_d$ ), whereas the LFC utilizes the moist adiabatic lapse rate (MALR;  $\Gamma_m$ ):

$$LCL = T_{parcel} - \frac{H}{\Gamma_d} \quad (9)$$

$$LFC = T_{parcel} - \frac{H}{\Gamma_m} \quad (10)$$

Figure 4.12 displays time series analysis of the difference in PBLH, LCL, and LCL deficit, spatially averaged over the burn scar extent and temporally averaged over all case days. The results from this analysis reveal important connections between LULC change and the depth of the PBL, as well as implications for cloud forcing (discussed further in section 4.2.4).

There appears to be an inverse relationship between the LCL and PBLH changes throughout the diurnal cycle over the burn scar. During the overnight hours while a NBL is in place the PBLH slightly increases post-fire compared to pre-fire, while the LCL decreases at most overnight time steps. The most substantial changes occurs during the daytime hours, where an increase of the LCL height by as much as 40 meters is noted, while a decrease in PBLH by up

to 20 meters occurs at the same time. The LFC changes post-fire are very similar to the response shown from the LCL (Figure 4.12). It is important to keep in mind that the average PBLH for the 15 case dates chosen for this study is ~ 700 meters above ground level (AGL), so these changes are quite noteworthy. Additionally, the LCL deficit, which is the vertical displacement of the LCL from the PBLH, also increases during the daytime and largely decreases at night. This indicates that over the burn scar extent, the mean effect of the LULC change on the LCL, PBLH, and LCL deficit is a daytime heating and drying effect and a smaller but still noteworthy nighttime saturating and cooling effect. The reduced moisture availability in the atmosphere also likely has an impact on the transpiration processes of remaining vegetation cover, further impacting the depth of the PBL. Further, the changes in LCL and LCL deficit suggest that there were changes in atmospheric stability over the burn scar, where increased instability during the daytime enhanced vertical motion thus altering  $\Gamma_{env}$  to be closer to the DALR while increased NBL stability at nighttime shifted the  $\Gamma_{env}$  to be closer to the MALR.

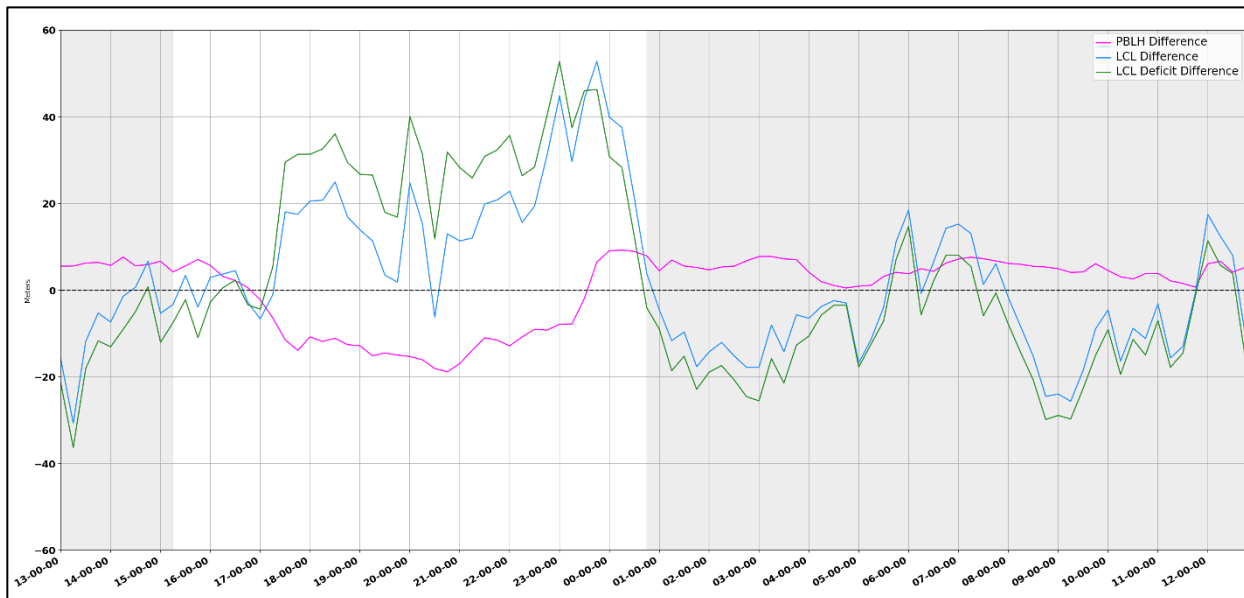


**Figure 4.12:** Run-averaged time series analysis of PBLH, LCL, and LCL deficit, spatially averaged over the Camp Fire burn scar extent.

#### 4.2.3.3. Wind and Mesoscale Circulations

Having established the LULC change-driven alterations boundary layer features such as temperature, moisture, and PBL depth, attention must now be directed to the resultant changes in wind speed and direction within the PBL across the burn scar domain. These results can help reveal whether mesoscale circulations, such as the slope-valley wind, have been altered in time, space, and/or strength by the removal of vegetation canopy across the burn scar.

Time-height visualizations were once again utilized to examine the progression and difference in the u-component of the wind, v-component of the wind, and total wind speed at four point locations following a latitudinal transect across the burn scar domain. These locations are: left edge of the burn scar (39.763, -121.781), Paradise, Buck's Lake, and right edge of the burn scar (39.763, -121.362). In examining these visualizations across the burn scar, it is evident that the slope-valley wind, which is a type of non-classical mesoscale circulation common to the study domain, experiences substantial changes post-fire.

The slope-valley wind is a local wind pattern that develops due to differential heating between the surface and free atmosphere at the same elevation some distance away. There are two components to the slope-valley wind, being the slope flow and valley winds, respectively. The slope-valley wind can be an important influence on a number of local meteorological conditions, such as air quality, frost and dew formation, convective triggers, fog development, temperature and moisture modifications, surface wind alterations, and turbulence potential. This mesoscale circulation is driven by diurnal heating cycles, and is most common in the summer to early fall. The circulation can be several hundred meters deep, and the average flow is  $\sim 3 - 6 \text{ ms}^{-1}$  (McNider and Pielke 1981, 1984). The slope-valley wind mesoscale circulation is most common under weak synoptic scale flow where vertical mixing is minimized. When upslope

flow is dominating, divergence within the valleys and convergence over elevated terrain can be expected, and the opposite is true for downslope-dominated hours. Additionally, LULC change can modify the underlying baroclinic gradients that drive the slope-valley wind mesoscale circulation (Phillips *et al.* 2022).

In the results of the WRF simulations, the strength of the slope-valley wind over the burn scar was seen to have slightly decreased from the early morning into the AET, where it then experiences a marked increase in strength throughout the nighttime hours. Figure 4.13 shows a time-height plot of the change in total wind speed at the Paradise point location, where the changes to the slope-valley wind stand out quite well from the surface to ~ 500 meters AGL. This net increase in the speed of the slope-valley wind was found through the remainder of the burn scar east of Paradise as well, and is indicative of the reduced friction near the surface as a result of the removal of the majority of the vegetation canopy.

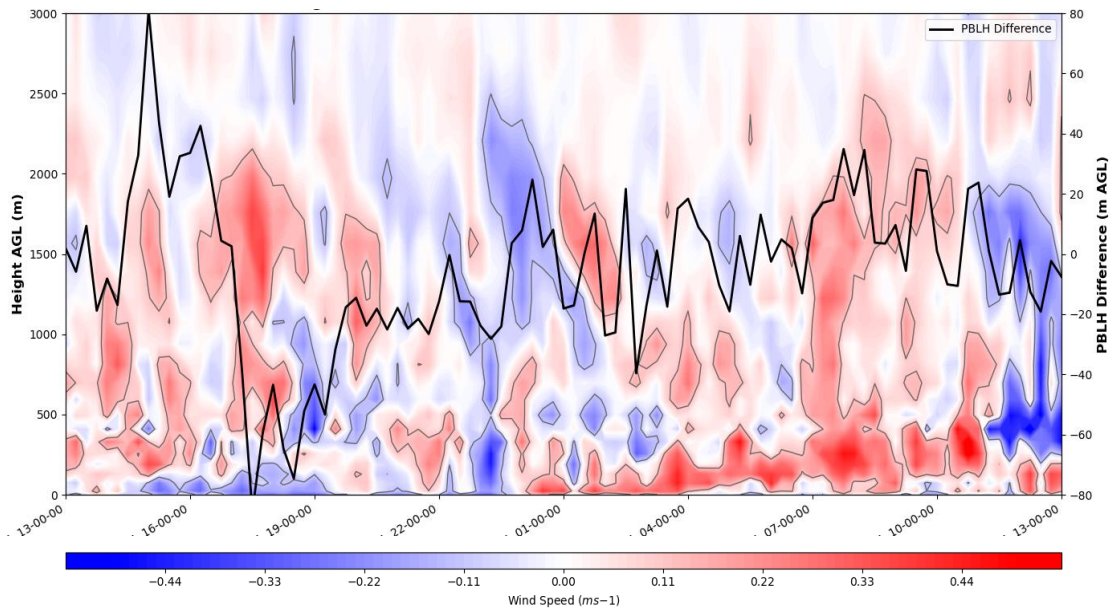


**Figure 4.13:** Run-averaged time-height plot at Paradise, CA of the difference in total wind post-fire compared to pre-fire. Note the changes to the strength of the slope-valley wind.

The direction of the slope-valley wind was also found to slightly change post-fire, with the most marked changes occurring from Paradise to the right edge of the burn scar. At Paradise, there was a positive change in the u-component of the wind, while at the right edge of the burn scar a negative decrease in the u-component of the wind was found. This indicates that an enhanced convergent zone may have set up post-fire between the two locations. In examining the Buck's Lake location (which is between Paradise and the right edge) this convergent pattern is revealed, with alternating positive and negative changes to the u-component of wind throughout time. Additionally, analysis of the average divergence of the 10 meter horizontal wind was examined to substantiate these results further. This analysis revealed that the simulations were correctly representing the slope-valley wind with convergent zones over heightened terrain and divergent zones over valleys during the day, and the opposite at night. These features were found to have been enhanced post-fire, as the strength of the circulation was increased.

In addition to the point location examinations, spatial analysis of the perturbation of the u-component, v-component, and total wind was examined at each time step for all case dates, as well as an average perturbation for each time step. The perturbation of the wind ( $U'$ ) is the difference between the instantaneous wind ( $U$ ) and mean wind ( $\bar{U}$ ), and can be computed for the u, v, and w components of wind as well as the total wind (Equation 11):

$$U' = U - \bar{U} . \quad (11)$$

These wind perturbations were examined as x-z cross sections taken across the central latitude of the innermost WRF domain, so that the core of the burn scar was in the center of the analysis. There were intricate wind patterns revealed in this analysis, mostly attributed to the complex terrain of the Sierra Nevada Mountains, which the burn scar resides on the foothills of. The most prominent changes to the perturbation wind occurred from Paradise to the Buck's Lake

area, which is where the most substantial LULC change occurred. The most marked changes to the perturbation wind were noted during peak heating hours over the east side of the burn scar, where the u-wind perturbation became slightly more positive through the PBL over the burned area while a much stronger negative response was coupled with it to the east (Figure B.1). This feature extended vertically several hundred meters AGL, and the Paradise area also saw a weaker and shallower but similar pattern to that of the east burn scar. These perturbation differences further build upon the findings of the alterations to the slope-valley wind being the most substantial over the most severely burnt areas.

The perturbation kinetic energy through the burn scar was also examined in the same fashion as that of the perturbation winds in order to compliment the findings of mesoscale circulation alterations. The changes to the perturbation kinetic energy were also the most notable over the same areas as that of the perturbation wind, indicating that the changes to energy as a result of the LULC change influenced the changes to mesoscale circulation features throughout the burn scar. Further, the highest pockets of surface-based perturbation kinetic energy were located over the plateau where Paradise resided, signifying a stronger connection to impervious surfaces. This connection is enhanced post-fire, as the vegetation canopy removal allowed for more direct radiative transfer from those otherwise sheltered surfaces.

Furthermore, run-averaged, diurnally averaged cross sections (through the PBL) and spatial (10 meters AGL) plots of u, v, and total wind were examined in order to tease out the overall changes in wind speed and direction across the burn scar post-fire compared to pre-fire conditions (Figure 4.14). These results find that both the u-wind and v-wind became more negative over the edges of the east portion of the burn scar extent at essentially the same magnitude (Figure 4.14 b, d), which indicates that the prevailing wind became more

northeasterly over the burn scar domain. The latitudinal cross section through the burn scar also reveals both the u and v-wind becoming more negative in the surface layer of the PBL from longitudes -121.6 to -121.4, with both components seeing a positive change around -121.7 (Figure 4.14 a, c). Though this is reflected in the 10-meter spatial difference plots- especially at and around Buck's Lake- the signal is stronger in the vertical pattern revealed in the cross sections. The change in the wind vectors was also examined to substantiate these discoveries, and it was found that the most substantial changes to the wind vectors occurred over the east portion of the burn scar domain, and became more northeasterly. Attention should also be brought to the fact that the prevailing wind for the majority of the burn scar was northeasterly in both pre- and post-fire simulations. Thus, the slope-valley mesoscale circulation was enhanced most directly in the slope wind portion of the circulation., as higher terrain resides in the east portion of the study domain. Further, these signals indicate that the spatial and vertical pattern in wind direction over the burn scar has changed most distinctly over the more severely altered LULC.

Overall, both the 10-meter u and v components of wind experienced a mean decrease of  $\sim -0.08$  and  $-0.06 \text{ ms}^{-1}$  over the burn scar extent, respectively (Table A.1). Further, the total wind difference in the PBL and lower FA (Figure 4.14 e) as well as the 10-meter wind spatial difference (Figure 4.14 f) show that the majority of the burn scar's surface layer experienced an increase in wind speed, with a mean 10-meter total wind difference of  $\sim 0.12 \text{ ms}^{-1}$  across the burn scar extent (Table A.1). This can once again be linked back to the friction of the surface being reduced by way of severe removal of the vegetation canopy.

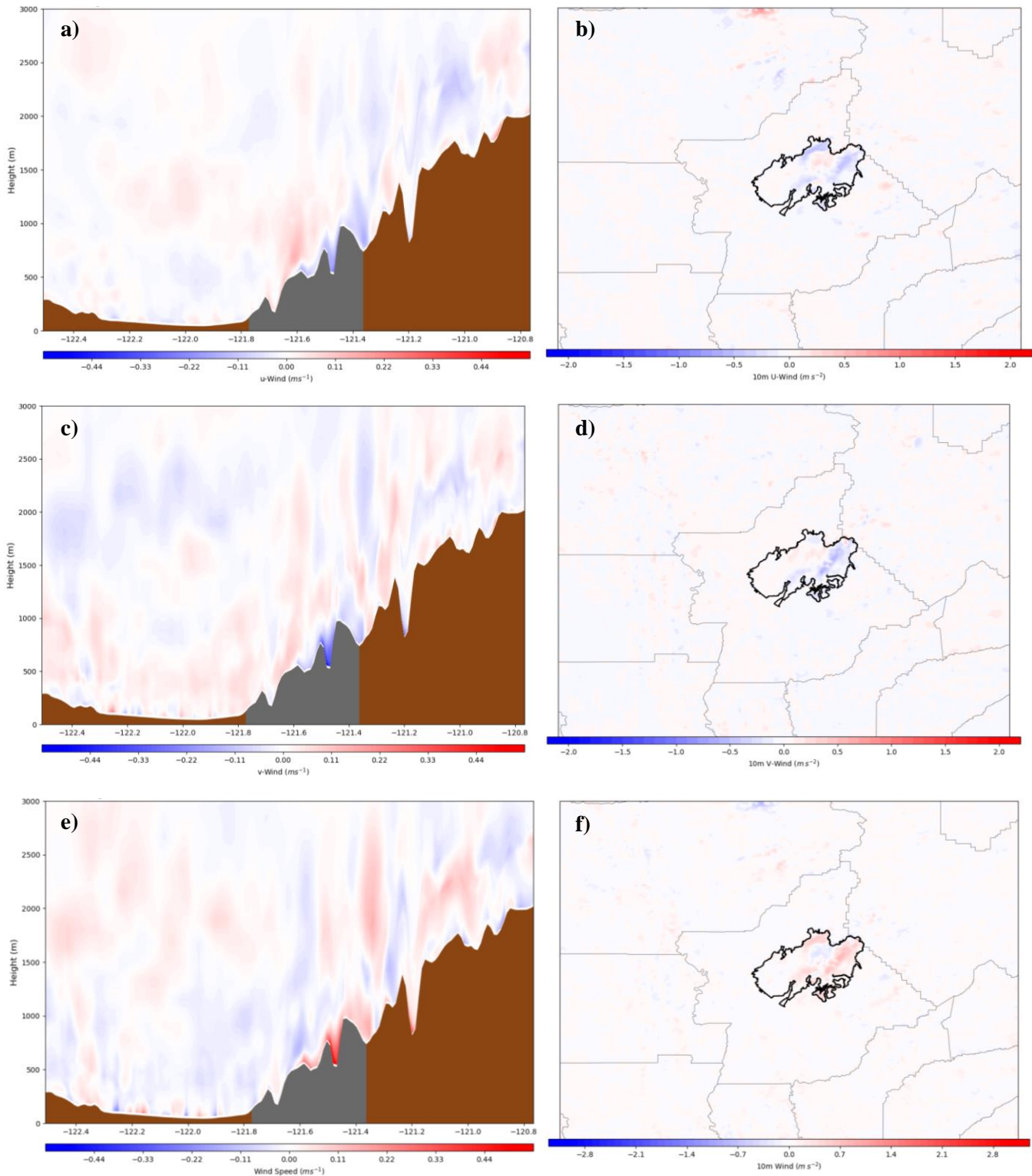


**Figure 4.14:** Run-averaged latitudinal x-z cross sections (a,c,e) and 10-meter x-y spatial (b,d,f) difference plots across the innermost WRF domain of the u (row 1) and v (row 2) components of wind as well as the total wind (row 3), showing post-fire minus pre-fire simulations. Plots are temporally averaged across one diurnal cycle. Brown shading in (a,c,e) is the terrain height in meters, with the dark grey shading being the location of the burn scar. The thick black outline in (b,d,f) is the extent of the burn scar perimeter.

In order to more fully understand how the changes in surface roughness impacted the friction and thus turbulent motion of wind across the burn scar extent, the changes in friction velocity ( $u^*$ ) post-fire compared to pre-fire were examined. Friction velocity is commonly applied in atmospheric science to characterize the momentum transfer between the Earth's surface and the atmosphere. Friction velocity can be derived from the equation for wind at a given height, which incorporates both the roughness length ( $z_0$ ) and the von Kármán constant ( $\kappa$ ), which can be approximated to 0.41 (Stull 1988; derived from Equation 9.7.1). By examining this relationship (Equation 12), conclusions about both  $u^*$  and  $z_0$  can be extracted:

$$u^* = \frac{\kappa \cdot U}{\ln\left(\frac{z}{z_0}\right)}. \quad (12)$$

The friction velocity was derived from WRF output using the 10-meter wind field (Figure 4.15). These results show that there was a complex response to surface roughness changes, with both prominent increases and decreases in friction velocity across the burn

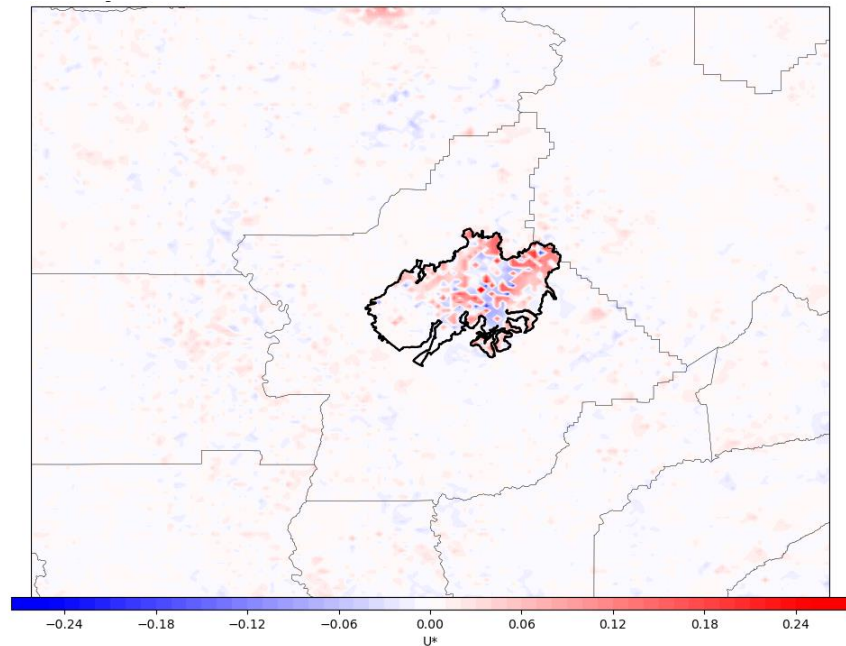


**Figure 4.15:** Run-averaged, spatial difference plots of the friction velocity over WRF domain 3, averaged over a 24-hour diurnal cycle from 13-13 UTC.

scar extent noted, but the overall mean across the burn scar revealed a statistically significant ( $p=0.05$ ) decrease in  $u^*$  by  $\sim 0.01$  (Table A.1). The revealed spatial pattern through the burn scar shows a close inverse spatial relationship to that of the albedo changes noted in section

4.2.1, indicating that the most severely burnt areas within the wildfire experienced a decrease in friction velocity and an increase in albedo, while the opposite was true for a quicker moving and cooler fire.

This net decrease in friction velocity, most visibly near the Buck's Lake area, is due to the impressive decrease in roughness length from upwards of a couple of meters in forest LULCs to as small as 0.1 meters over grassland LULCs (Stull 1988). This drastic change in roughness length was verified by examining the Light Detection and Ranging (LiDAR)-derived Geoscience Laser Altimeter System (GLAS) and Global Ecosystem Dynamics Investigation (GEDI) vegetation height products from 2005 and 2019 respectively, which revealed that the most severely burnt regions within the burn scar saw a decrease of average canopy height from over 15 meters to less than 1 meter.

In summary, wildfire-driven LULC changes have immense consequences on the local weather and climate conditions within the PBL, causing warmer and drier conditions, temporal changes to the depth of the boundary layer, and temporal and spatial changes to wind speed and direction (and thus alterations in mesoscale circulations such as the slope-valley wind). All of these variations have implications in how cloud forcing and precipitation patterns will behave post-fire, which are discussed in section 4.2.4.

#### **4.2.4. Modeled Changes in Cloud Forcing and Precipitation**

The final set of results pertinent to examine for this study are the modeled changes in cloud forcing and precipitation across and adjacent to the burn scar extent. Exploring these results have important implications for water levels, quality, and sediment load of nearby reservoirs such as Lake Oroville, changes in drought and flood risk, and erosion of the watersheds within and nearby the burn scar.

First, the changes in cloud forcing across and adjacent to the burn scar post-fire compared to pre-fire were examined. The overall maximum cloud fraction as well as maximum low, middle, and high cloud fractions were all examined across the pre-defined diurnal cycle, for all case dates. Cloud fraction was derived by finding the maximum relative humidity within certain pressure ranges for each cloud level as defined by the National Center for Atmospheric Research (NCAR), and applying NCAR's equations for cloud fraction per the wrf-python package for each cloud level (NCAR Computational and Information Systems Laboratory 2021). Low and middle cloud fractions were derived using Equation 13 and high cloud fraction was derived using Equation 14:

$$CFRAC = 4.0 * RH_{max} - 3.0 \quad (13)$$

$$CFRAC = 2.5 * RH_{max} - 1.5 \quad (14)$$

The NCAR pressure bins for each cloud level are as follows: 97000 Pa <= low clouds < 80000 Pa middle clouds < 45000 Pa high clouds. Overall, the low cloud layer saw the most substantial changes, with an average increase in cloud fraction over the burn scar extent of ~ 0.23 % (p < 0.01) and an increase elsewhere throughout WRF domain 3 of just under 0.1 % (Table A.1). The middle cloud layer also saw an average increase in cloud fraction of ~ 0.12 % over the burn scar and ~ 0.05 % outside of the burn scar, while the high cloud layer remained essentially unchanged from pre-fire to post-fire conditions (Table A.1).

The spatial patterns of these run-averaged changes across the entire diurnal cycle reveal interesting patterns over and adjacent to the burn scar extent. The entirety of the burn scar extent saw a trivial increase in low cloud layer fraction, with this positive corridor extending to the northwest and southeast of the scar as well (Figure 4.16 a). This spatial pattern corresponds nicely to the increase in terrain from west to east across the domain as the foothills of the Sierra

Nevada mountains begin to rise. The changes to LULC leading to changes in the energy balance (section 4.2.2) coupled with orographic forcing are the main drivers of this pattern. Nevertheless, the LCL and PBLH changes noted in section 4.2.3 indicate daytime drying of the boundary layer, which would suppress cloud development during the daytime hours. However, the time series analysis of mean cloud fraction difference shows a slight increase throughout the entire diurnal cycle (Figure 4.16 b). Additionally, the divergence of the 10-meter horizontal wind for the precipitating case dates revealed enhanced convergence over the eastern portion of the burn scar post-fire, thus allowing for vertical motion favorable to cloud formation.

Further, the mean middle cloud layer fraction difference also shows an overall increase across the burn scar, but with more spatial variability surrounding the scar- even with a noted decrease in the north-central portion of the scar. This decrease could be related to changes in vertical fluxes in proximity to the city of Paradise (Figure 4.6), and is also very close spatially to where wind shifts occur post-fire (Figure 4.13). Though there is no strong signal in the mean difference of high cloud layer fraction spatially, the overall changes through the entire depth of the atmospheric column show the highest cloud fraction increase occurring over the area where the hottest FRP of the Camp Fire was measured.

The previously defined hours of daytime and nighttime were also examined separately to determine when cloud fraction changes were most prevalent, and these results revealed that the largest increases in cloud cover were during the daytime within the low and middle layers; these increases were only upwards of 0.075%, which is statistically insignificant. There were net decreases in cloud fraction during the nighttime hours at both the low and middle layers over the burn scar, but once again these changes were not significant. Overall, these changes in cloud fraction are quite miniscule and the variation across all case dates is quite high (Figure 4.16 d, e,

f), so further examination into shallow cumulus or isolated thunderstorm development over and near the burn scar are needed to capture the entire impact of drastic LULC change on cloud forcing.

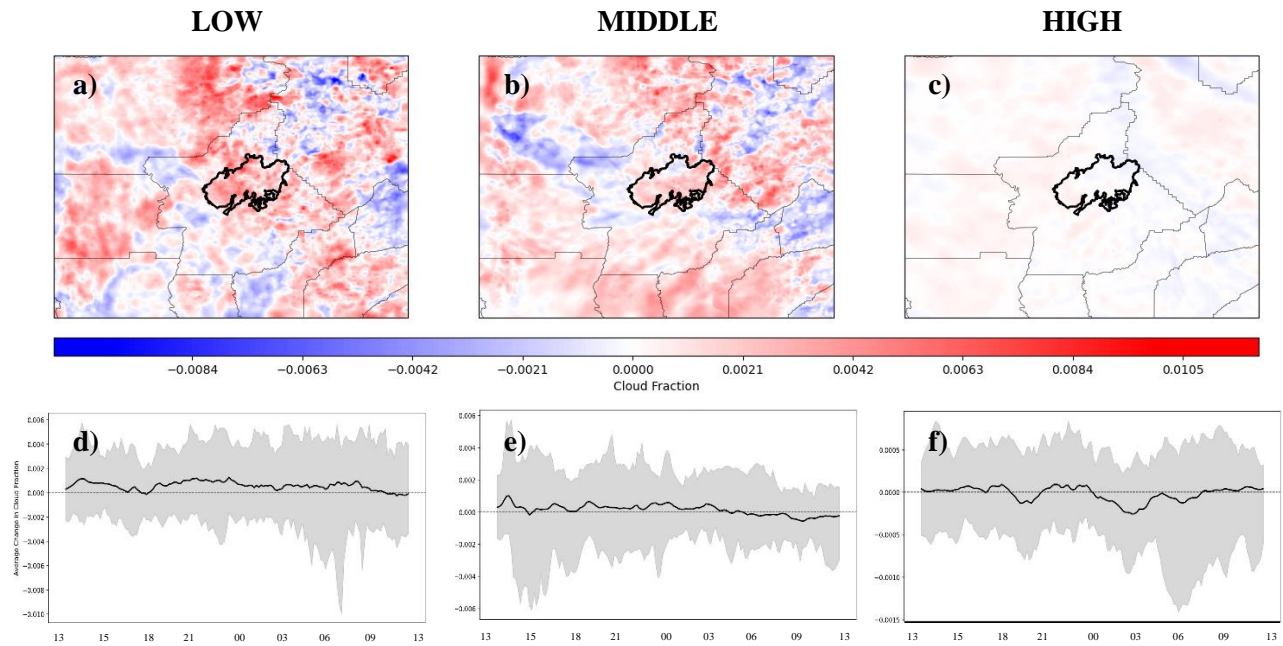


**Figure 4.16:** Run-averaged mean spatial difference plots of low, middle, and high cloud layer fraction. Values here are shown in the range 0-1.

The final set of results pertinent to be examined for this study were that of the changes in precipitation patterns across and adjacent to the burn scar. Though only a handful of the case days selected for this study included noteworthy precipitation, initial results could still be construed. The quantitative precipitation forecast (QPF) accumulated over the entire 36-hour simulation was analyzed in this segment of the results to capture a comprehensive overview of any alterations. The Advanced Hydrologic Prediction Service (AHPS) 24-hour QPF product was also utilized for this portion of the analysis in order to validate model output. In the precipitating case dates, the general patterns of rainfall were present in both the AHPS and modeled fields, and though the modeled simulations produced slightly more precipitation than AHPS observed, post-fire results were closer to the observations than pre-fire simulated results.

In examining the QPF footprints of all case days that produced noteworthy precipitation, as well as their changes, the largest differences occurred downwind of the burn scar, where obvious decreases

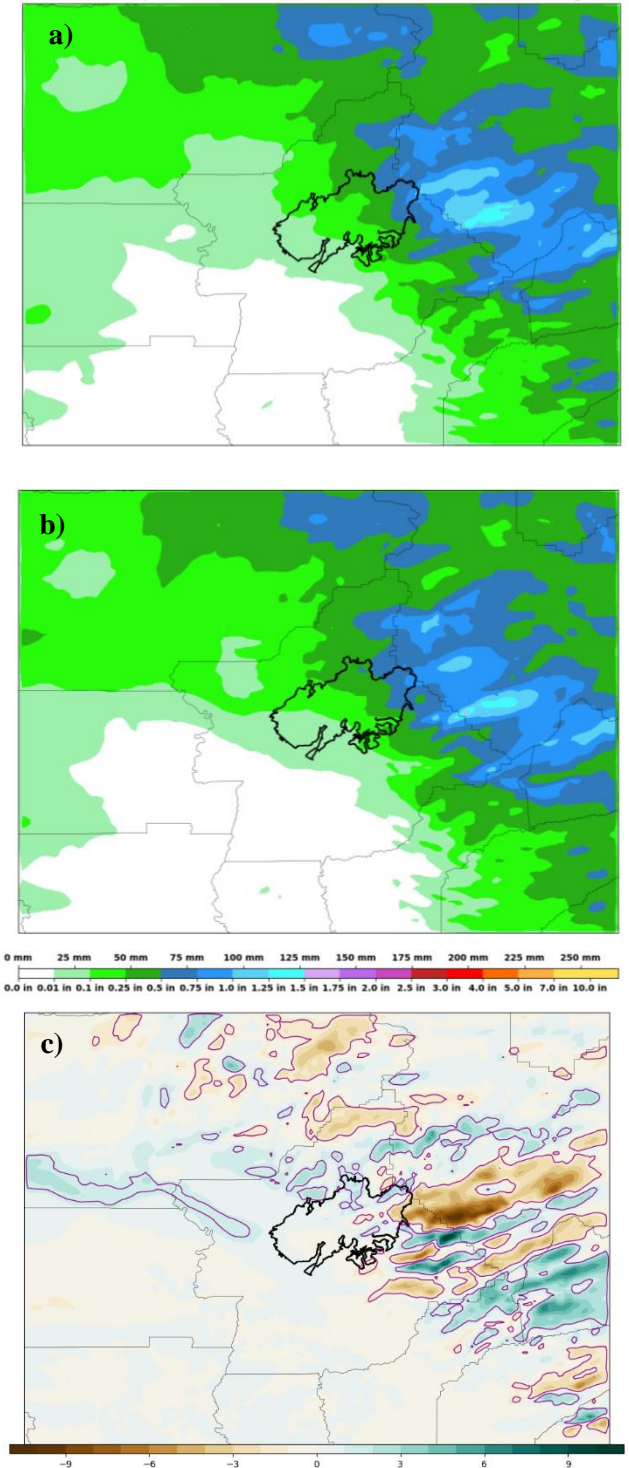


**Figure 4.17:** Example WRF convective case date (November 30, 2018) showing the pre-fire and post-fire accumulated rainfall footprints (a, b), as well as the difference post-fire compared to pre-fire (c). The magenta lines on c are areas where the difference is greater than 1 std of the mean.

in precipitation were noted. Figure 4.17 shows a clear example case date of this forcing (30 November 2018), where post-fire simulations resulted in over 5 mm less precipitation downwind of the burn scar compared to pre-fire simulations. The main culprit of this reduction in widespread precipitation downwind of the burn scar extent is once again tied back to the reduction in available moisture content in the atmosphere over the burn scar. The (predominately daytime) drying of the boundary layer post-fire compared to pre-fire conditions could have consequences on the precipitation footprints near and over the burn scar. However, the increase in Day LST and near-surface temperature thereby increased instability in post-fire conditions, which has been proven to allow for any sustained convection to become reinvigorated as it passed over the burn scar. Overall, the primary effect of LULC change as a result of a wildfire on local cloud and precipitation forcing found from this study is a reduction of precipitation downwind of the burn scar, especially in areas of complex terrain features. This response is similar to that of urbanization nearby complex terrain, as both local atmospheres see similar temperature and moisture responses post-fire and post-urbanization (Freitag *et al.* 2018).

In examining the wind vectors for both pre- and post-fire simulations over all case dates that produced precipitation over or near the burn scar, increased convergence was noted downwind of the burn scar, which could help organize precipitation patterns into isolated and potentially reinvigorated convection. Though some small pockets of concentrated QPF were noted within the larger stratiform footprint downwind of the burn scar post-fire in two of the precipitation-producing case dates, no widespread shallow cumulus or isolated thunderstorm cases were simulated for this study. Future investigations into this phenomena will be needed to validate results of prior studies that reveal convective reinvigoration downwind of burn scars (Anthes 1984; Chen *et al.* 2001; Cutrim *et al.* 1995; Molders and Kramm 2007; Page 2007) as

well as examine complex terrain's impact on convective cores when coupled with drastic LULC change.

Finally, it should be noted that in the cases chosen for this study, orographic lift along the foothills of the Sierra Nevada mountains did play an important role in forcing precipitation and determining the location of their footprints. This relationship between orographic effects and LULC change will also need to be examined further in future studies.

## Chapter 5. Conclusions

As the implications of human impact from wildfire events continues to increase due to rapidly expanding development conjoined with recent increasing trends in fire frequency and burned area, the LULC changes as a result of these severe weather events will play a progressively more substantial role in localized alterations in weather and climate. Hence, this thesis explores the changes to land-atmosphere interactions from the 2018 Camp Fire in northern California by answering the following questions:

1. How does severe removal of vegetation impact the local surface energy balance?
2. What are the impacts of drastic changes in LULC to localized mesoscale circulation development?
3. What are the downstream effects on cloud formation and precipitation footprints as a result of localized yet drastic LULC changes?

The answers found to these questions can be utilized to inform a vast array of policies and provide valuable insight for future scientific advancements in weather and climate resilience as well as land management.

The analysis of the results of this study revealed significant transformations in land surface properties post-wildfire, specifically decreases in greenness fraction / NDVI, increases in albedo, and large increases in LST. The simulated changes to these variables closely mirrored the observed differences from MODIS-derived data. Notably, variations in albedo exhibited spatial complexity, influenced by LULC-specific changes, such as the shift from dwarf scrub to pasture compared to urban to pasture. From these substantial alterations to land surface properties, the

local surface energy budget was considerably modified. The SH experienced a large increase while the LE saw a comparable decrease of a slightly smaller magnitude, particularly over the eastern extent of the burn scar. Additionally, the total net radiation over the burn scar was reduced by an average of  $0.2 \text{ MJ m}^{-2}$ , and the net radiation at peak heating was reduced by 50 to as much as  $175 \text{ Wm}^{-2}$ . The main driver of this reduction in net radiation was the increase in upwelling solar radiation of  $\sim 60\text{-}80 \text{ Wm}^{-2}$  across the burn scar extent. For question 1, the hypothesis of the influence of burn scar-induced LULC changes on land surface properties and thus the local surface energy balance was confirmed.

The study further unveiled substantial modifications in local boundary layer features, including but not limited to temperature, moisture, PBL depth, and wind speed and direction. The DTR over the burn scar domain was found to have increased, emphasizing the daytime heating and nighttime cooling effects of post-fire LULC. Time-height analysis at several locations across the study area illustrated the dynamic relationship between temperature, moisture, wind, and the PBLH, emphasizing the importance of LULC alterations in influencing changes to these variables. An increase in wind speed and shift to a more northeasterly direction were observed, particularly in relation to the near surface slope-valley wind mesoscale circulation. The reduction in surface roughness due to drastic removal of vegetation canopy across the burn scar played a large role in modifying wind characteristics, influencing the observed changes in both speed and direction. For question 2, the hypothesis proposing LULC changes driving significant impacts on local boundary layer features and wind patterns, thus leading to changes to mesoscale circulations, were also confirmed.

Finally, the investigation into cloud forcing and precipitation patterns as well as their downstream hydrologic impacts highlights nuanced responses to LULC change across the burn

scar domain. Low cloud fractions slightly increased over the burn scar, influenced by both orographic effects and alterations in the local energy balance. Daytime drying of the boundary layer post-fire did not have a strong impact on cloud development over the burn scar, but only primarily stratiform days were examined, so future research into shallow cumulus and isolated thunderstorm cases will need to be investigated. Precipitation patterns showed decreases downwind of the burn scar, emphasizing the role of reduced moisture availability. The precipitation response to the presence of the burn scar was similar to that of rapid urbanization, in that reduced moisture and increased temperature over this domain led to downwind decreases in precipitation but reorganization into smaller convective cores post-fire. This response becomes more complicated by the existence of complex terrain downwind of the burn scar. The vast majority of California's wildfires from 1984 to the present have been collocated with complex terrain features, so the implications of these results can be applied to numerous locations through the state as well as at other locations worldwide. For question 3, the hypothesis anticipating shifts in cloud forcing and resultant precipitation patterns were partially validated, but further research is necessary to completely answer the question posed.

Overall, these findings carry profound implications for, among other areas, water resource management, drought and flood risk assessment, and erosion control in regions affected by wildfires. Understanding the intricate dynamics of LULC change-induced alterations in local weather and climate patterns allows for more informed decision making in land-use planning and environmental conservation efforts in areas susceptible to frequent wildfire risk. To the author's knowledge, this is the most comprehensive analysis to date of the land-atmosphere system's response to burn scars. This study's results are pertinent to ongoing investigations into disaster risk mitigation, land management practices, and even numeric modeling experiments of similar

nature. Thus, the outcome of this investigation is important for fully understanding and addressing the broader implications of wildfires on the environment, informing sustainable land management strategies and enhancing resilience in regions susceptible to frequent wildfire risk.

Future research should delve deeper into the interactions between wildfire-driven LULC changes and precipitation, exploring the role of atmospheric stability, wind patterns, and orographic effects – especially in isolated to scattered thunderstorm cases. Investigating the consequences of these changes on local ecosystems and water resources will contribute to developing strategies for sustainable land management in fire-prone regions across the world. Additionally, this study underscores the imperative of delving into the lasting repercussions of wildfire-induced LULC changes beyond the immediate post-fire period, stressing the necessity for further research to comprehensively address the longer-term implications of wildfire-induced burn scars on the land-atmosphere system.

## References

- Anthes, R., 1984: Enhancement of Convective Precipitation by Mesoscale Variations in Vegetative Covering in Semiarid Regions. *J Appl Meteorol Climatol*, **23**, 541–554.
- Arakawa, A., and V. R. Lamb, 1977: Computational design of the basic dynamical processes of the UCLA general circulation model. *Methods in Computational Physics: Advances in Research and Applications*.
- Barthlott, C., U. Corsmeier, C. Meißner, F. Braun, and C. Kottmeier, 2006: The influence of mesoscale circulation systems on triggering convective cells over complex terrain. *Atmos Res*, **81**, 150–175, <https://doi.org/10.1016/j.atmosres.2005.11.010>.
- Berg, L. K., W. I. Gustafson, E. I. Kassianov, and L. Deng, 2013: Evaluation of a modified scheme for shallow convection: Implementation of CuP and case studies. *Mon Weather Rev*, **141**, 134–147, <https://doi.org/10.1175/MWR-D-12-00136.1>.
- Bolton, D., 1980: The Computation of Equivalent Potential Temperature. *Mon Weather Rev*, **108**.
- Brewer, M. J., and C. B. Clements, 2020: The 2018 camp fire: Meteorological analysis using in situ observations and numerical simulations. *Atmosphere (Basel)*, **11**, <https://doi.org/10.3390/ATMOS11010047>.
- Cannon, S. H., and J. DeGraff, 2009: The increasing wildfire and post-fire debris-flow threat in western USA, and implications for consequences of climate change. *Landslides: Disaster Risk Reduction*.
- Cannon, S. H., R. M. Kirkham, and M. Parise, 2001: Wildfire-related debris-flow initiation processes, Storm King Mountain, Colorado. *Geomorphology*, **39**, 171–188.
- Charney, J. G., 1975: Dynamics of deserts and drought in the Sahel. *Quarterly Journal Royal Meteorological Society*, **101**, 193–202.

- Chen, F., T. T. Warner, and K. Manning, 2001: *Sensitivity of Orographic Moist Convection to Landscape Variability: A Study of the Buffalo Creek, Colorado, Flash Flood Case of 1996*.
- Chen, J., L. A. Pangle, J. P. Gannon, and R. D. Stewart, 2020: Soil water repellency after wildfires in the Blue Ridge Mountains, United States. *International Journal of Wildland Fire*, **29**, 1009–1020.
- Chen, Y., and Coauthors, 2022: California wildfire spread derived using VIIRS satellite observations and an object-based tracking system. *Sci Data*, **9**, <https://doi.org/10.1038/s41597-022-01343-0>.
- Chow, F. K., and Coauthors, 2022: High-Resolution Smoke Forecasting for the 2018 Camp Fire in California. *Bull Am Meteorol Soc*, **103**, E1531–E1552, <https://doi.org/10.1175/BAMS-D-20-0329.1>.
- Claverie, M., J. Ju, J. G. Masek, J. L. Dungan, E. F. Vermote, J. C. Roger, S. V. Skakun, and C. Justice, 2018: The Harmonized Landsat and Sentinel-2 surface reflectance data set. *Remote Sens Environ*, **219**, 145–161, <https://doi.org/10.1016/j.rse.2018.09.002>.
- Cochrane, M. A., C. J. Moran, M. C. Wimberly, A. D. Baer, M. A. Finney, K. L. Beckendorf, J. Eidenshink, and Z. Zhu, 2012: Estimation of wildfire size and risk changes due to fuels treatments. *Int J Wildland Fire*, **21**, 357–367, <https://doi.org/10.1071/WF11079>.
- Cutrim, E., D. W. Martin, and R. Rabin, 1995: *Enhancement of Cumulus Clouds over Deforested Lands in Amazonia*.
- Debano, L. F., *The role of fire and soil heating on water repellency in wildland environments: a review*. [www.elsevier.com/locate/jhydrol](http://www.elsevier.com/locate/jhydrol).
- Dennis Staley, B. M., J. A. Negri, J. W. Kean, J. M. Laber, A. C. Tillery, A. M. Youberg, and S. M. Kimball, Updated Logistic Regression Equations for the Calculation of Post-Fire Debris-Flow Likelihood in the Western United States. <https://doi.org/10.3133/ofr20161106>.
- DiBiase, R. A., and M. P. Lamb, 2020: Dry sediment loading of headwater channels fuels post-wildfire debris flows in bedrock landscapes. *Geology*, **48**, 189–193, <https://doi.org/10.1130/G46847.1>.

- Didan, K., and A. Barreto Munoz, 2015: *MODIS Vegetation Index User's Guide (MOD13 Series)*.  
<https://vip.arizona.edu>.
- Eidenshink, J., B. Schwind, K. Brewer, Z.-L. Zhu, B. Quayle, and S. Howard, 2007: *A PROJECT FOR MONITORING TRENDS IN BURN SEVERITY*. <http://www.fi>.
- Fan, L., P. Lehmann, B. McArdell, and D. Or, 2017: Linking rainfall-induced landslides with debris flows runout patterns towards catchment scale hazard assessment. *Geomorphology*, **280**, 1–15,  
<https://doi.org/10.1016/j.geomorph.2016.10.007>.
- Francos, M., and X. Úbeda, 2021: Prescribed fire management. *Curr Opin Environ Sci Health*, **21**,  
<https://doi.org/10.1016/j.coesh.2021.100250>.
- Freitag, B. M., U. S. Nair, and D. Niyogi, 2018: Urban Modification of Convection and Rainfall in Complex Terrain. *Geophys Res Lett*, **45**, 2507–2515, <https://doi.org/10.1002/2017GL076834>.
- Gartner, J. E., S. H. Cannon, and P. M. Santi, 2014: Empirical models for predicting volumes of sediment deposited by debris flows and sediment-laden floods in the transverse ranges of southern California. *Eng Geol*, **176**, 45–56, <https://doi.org/10.1016/j.enggeo.2014.04.008>.
- Grell, G. A., and S. R. Freitas, 2014: A scale and aerosol aware stochastic convective parameterization for weather and air quality modeling. *Atmos Chem Phys*, **14**, 5233–5250, <https://doi.org/10.5194/acp-14-5233-2014>.
- Hernandez, C., P. Drobinski, and S. Turguety, 2015: Impact of wildfire-induced land cover modification on local meteorology: A sensitivity study of the 2003 wildfires in Portugal. *Atmos Res*, **164–165**, 49–64.
- Homer, C., and N. Hossain, 2007: *Completion of the 2001 National Land Cover Database for the Conterminous United States*. <https://www.researchgate.net/publication/237239863>.

- , and L. Yang, 2015: Completion of the 2011 National Land Cover Database for the Conterminous United States-Representing a Decade of Land Cover Change Information.  
<https://doi.org/10.14358/PERS.81.5.345>.
- Homer, C. H., J. A. Fry, and C. A. Barnes, 2012: The National Land Cover Database, U.S. Geological Survey Fact Sheet.
- Hong, S.-Y., Y. Noh, and J. Dudhia, 2006: *A New Vertical Diffusion Package with an Explicit Treatment of Entrainment Processes*.
- Hu, L., and N. A. Brunzell, 2013: The impact of temporal aggregation of land surface temperature data for surface urban heat island (SUHI) monitoring. *Remote Sens Environ*, **134**, 162–174,  
<https://doi.org/10.1016/j.rse.2013.02.022>.
- Hubbert, K. R., P. M. Wohlgemuth, J. L. Beyers, M. G. Narog, and R. Gerrard, 2012: Post-fire soil water repellency, hydrologic response, and sediment yield compared between grass-converted and chaparral watersheds. *Fire Ecology*, **8**, 143–162, <https://doi.org/10.4996/fireecology.0802143>.
- Janjic, Z. I., 1994: The Step-Mountain Eta Coordinate Model: Further Developments of the Convection, Viscous Sublayer, and Turbulence Closure Schemes. *Mon Weather Rev*,.
- Kain, J. S., 2004: *The Kain-Fritsch Convective Parameterization: An Update*.
- Knapp, E. E., Y. S. Valachovic, S. L. Quarles, and N. G. Johnson, 2021: Housing arrangement and vegetation factors associated with single-family home survival in the 2018 Camp Fire, California. *Fire Ecology*, **17**, <https://doi.org/10.1186/s42408-021-00117-0>.
- Knowles, C. J. B., 1993: *The influence of forest fire induced albedo differences on the generation of mesoscale circulations*.
- Langland, R. H., and C.-S. Liou, 1996: Implementation of an E-ε Parameterization of Vertical Subgrid-Scale Mixing in a Regional Model. *Mon Weather Rev*,.
- Lizzie Johnson, 2021: *Paradise: One Town's Struggle to Survive an American Wildfire*. Crown Trade,.

- Mass, C. F., and D. Ovens, 2021: The Synoptic and Mesoscale Evolution Accompanying the 2018 Camp Fire of Northern California. *Bull Am Meteorol Soc*, **102**, E168–E192, <https://doi.org/10.1175/BAMS-D-20-0124.1>.
- May, C. L., and R. E. Gresswell, 2004: Spatial and temporal patterns of debris-flow deposition in the Oregon Coast Range, USA. *Geomorphology*, **57**, 135–149, [https://doi.org/10.1016/S0169-555X\(03\)00086-2](https://doi.org/10.1016/S0169-555X(03)00086-2).
- May, R. M., and Coauthors, 2022: MetPy: A Meteorological Python Library for Data Analysis and Visualization. *Bull Am Meteorol Soc*, **103**, E2273–E2284, <https://doi.org/10.1175/BAMS-D-21-0125.1>.
- McCumber, M. C., 1980: A NUMERICAL SIMULATION OF THE INFLUENCE OF HEAT AND MOISTURE FLUXES UPON MESOSCALE CIRCULATIONS.
- McNider, R. T., and R. A. Pielke, 1981: Diurnal Boundary-Layer Development over Sloping Terrain. *J Atmos Sci*.
- , and —, 1984: Numerical Simulation of Slope and Mountain Flows. *Journal of Climate and Applied Meteorology*.
- , and A. Pour-Biazar, 2020: Meteorological modeling relevant to mesoscale and regional air quality applications: a review. *J Air Waste Manage Assoc*, **70**, 2–43, <https://doi.org/10.1080/10962247.2019.1694602>.
- McPherson, R. A., 2007: A review of vegetation–atmosphere interactions and their influences on mesoscale phenomena. *Prog Phys Geog*, **31**, 261–285.
- Molders, N., and G. Kramm, 2007: Influence of wildfire induced land cover changes on clouds and precipitation in Interior Alaska. *Atmos Res*, **84**, 142–168.

Nakanishi, M., and H. Niino, 2006: An improved Mellor-Yamada Level-3 model: Its numerical stability and application to a regional prediction of advection fog. *Boundary Layer Meteorol*, **119**, 397–407, <https://doi.org/10.1007/s10546-005-9030-8>.

National Center for Atmospheric Research Computational and Information Systems Laboratory, 2021: Geoscience Community Analysis Toolkit: WRF-Python.

Ookouchi Y., M. Segal, R. Kessler, and R. Pielke, 1984: Evaluation of Soil Moisture Effects on the Generation and Modification of Mesoscale Circulations. *Mon Weather Rev*, **112**, 2281–2292, [https://doi.org/https://doi.org/10.1175/1520-0493\(1984\)112%3C2281:EOSMEO%3E2.0.CO;2](https://doi.org/https://doi.org/10.1175/1520-0493(1984)112%3C2281:EOSMEO%3E2.0.CO;2).

Page, E. M., 2007: Post-fire impacts on microclimate and convective precipitation. Colorado State University, .

Parise, M., and S. H. Cannon, 2012: Wildfire impacts on the processes that generate debris flows in burned watersheds. *Natural Hazards*, **61**, 217–227, <https://doi.org/10.1007/s11069-011-9769-9>.

Phillips, C. E., U. S. Nair, R. Mahmood, E. Rappin, and R. A. Pielke, 2022: Influence of Irrigation on Diurnal Mesoscale Circulations: Results From GRAINEX. *Geophys Res Lett*, **49**, <https://doi.org/10.1029/2021GL096822>.

Pielke, R. A., and R. Avissar, 1990: Influence of landscape structure on local and regional climate. *Landsc Ecol*, **4**, 133–155, <https://doi.org/10.1007/BF00132857>.

Pielke, R. A., W. A. Lyons, R. T. McNider, M. D. Moran, D. A. Moon, R. A. Stocker, R. L. Walko, and M. Uliasz, 1991: Regional and mesoscale meteorological modeling as applied to air quality studies. *Air pollution modeling and its application* , Vol. VIII of.

Prochaska, A. B., P. M. Santi, J. D. Higgins, and S. H. Cannon, 2008: Debris-flow runout predictions based on the average channel slope (ACS). *Eng Geol*, **98**, 29–40, <https://doi.org/10.1016/j.enggeo.2008.01.011>.

- Purser, R. J., and L. M. Leslie, 1988: A Semi-Implicit, Semi-Lagrangian Finite-Difference Scheme Using High-Order Spatial Differencing on a Nonstaggered Grid. *Mon Weather Rev.*
- Rabin, R. M., S. Stadler, P. J. Wetzel, P. J. Stensrud, and M. Gregory, 1990: *Observed Effects of Landscape Variability on Convective Clouds.*
- Renno, N. O., R. Renno, M. L. Burkett, and M. P. Larkin, 1998: *A Simple Thermodynamical Theory for Dust Devils.*
- Renno, N. O., and A. P. Ingersoll, 1996: Natural Convection as a Heat Engine: A Theory for CAPE. *J Atmos Sci.*
- Rooney, B., Y. Wang, J. H. Jiang, B. Zhao, Z. C. Zeng, and J. H. Seinfeld, 2020: Air quality impact of the Northern California Camp Fire of November 2018. *Atmos Chem Phys*, **20**, 14597–14616, <https://doi.org/10.5194/acp-20-14597-2020>.
- Santanello, J. A., and Coauthors, 2018: Land-atmosphere interactions the LoCo perspective. *Bull Am Meteorol Soc*, **99**, 1253–1272, <https://doi.org/10.1175/BAMS-D-17-0001.1>.
- Schulze, S. S., E. C. Fischer, S. Hamideh, and H. Mahmoud, 2020: Wildfire impacts on schools and hospitals following the 2018 California Camp Fire. *Natural Hazards*, **104**, 901–925, <https://doi.org/10.1007/s11069-020-04197-0>.
- Segal, M., R. Avissar, M. C. McCumber, and R. A. Pielke, 1988: Evaluation of Vegetation Effects on the Generation and Modification of Mesoscale Circulations. *J Atmos Sci.*
- Segal, M., R. W. Arritt, and L. ' Kansas66045, 1992: *Nonclassical Mesoscale Sensible Heat-Flux Gradients.*
- Silva Dias, M. A. F. R. P., 1996: Simulation of mesoscale circulations in a deforested area of Rondonia in the dry season. *Amazonian Deforestation and Climate*, 531–547.
- Simms, L. A., E. Borrás, B. S. Chew, B. Matsui, M. M. McCartney, S. K. Robinson, N. Kenyon, and C. E. Davis, 2021: Environmental sampling of volatile organic compounds during the 2018 Camp Fire in Northern California. *J Environ Sci (China)*, **103**, 135–147, <https://doi.org/10.1016/j.jes.2020.10.003>.

- Souza, E. P., N. O. Renno, and M. A. F. S. Dias, 2000a: Convective circulations induced by surface heterogeneities. *J Atmos Sci*, **57**, 2915–2922, [https://doi.org/10.1175/1520-0469\(2000\)057<2915:CCIBSH>2.0.CO;2](https://doi.org/10.1175/1520-0469(2000)057<2915:CCIBSH>2.0.CO;2).
- Spearing, L. A., and K. M. Faust, 2020: Cascading system impacts of the 2018 Camp Fire in California: The interdependent provision of infrastructure services to displaced populations. *International Journal of Disaster Risk Reduction*, **50**, <https://doi.org/10.1016/j.ijdr.2020.101822>.
- Sridhar, V., R. L. Elliott, F. Chen, and J. A. Brotzge, 2002: Validation of the NOAA-OSU land surface model using surface flux measurements in Oklahoma. *Journal of Geophysical Research: Atmospheres*, **107**, ACL 3-1-ACL 3-18, <https://doi.org/10.1029/2001JD001306>.
- Staley, D. M., J. A. Negri, J. W. Kean, J. L. Laber, A. C. Tillery, and A. M. Youberg, 2017: Prediction of spatially explicit rainfall intensity–duration thresholds for post-fire debris-flow generation in the western United States. *Geomorphology*, **278**, 149–162, <https://doi.org/10.1016/J.GEOMORPH.2016.10.019>.
- Stephens, S. L., R. E. Martin, and N. E. Clinton, 2007: Prehistoric fire area and emissions from California’s forests, woodlands, shrublands, and grasslands. *For Ecol Manage*, **251**, 205–216, <https://doi.org/10.1016/j.foreco.2007.06.005>.
- Strahler, A. H., and J. P. Muller, 1999: MODIS BRDF Albedo Product : Algorithm Theoretical Basis Document. *MODIS Product ID: MOD43, Version 5.*, 1–53.
- Stull, R. B., 1988: *An Introduction to Boundary Layer Meteorology*.
- Takahashi, T., *ESTIMATION OF POTENTIAL DEBRIS FLOWS AND THEIR HAZARDOUS ZONES; SOFT COUNTERMEASURES FOR A DISASTER*.
- Tryhorn, L., A. Lynch, R. Abramson, and K. Parkyn, 2008: On the meteorological mechanisms driving postfire flash floods: A case study. *Mon Weather Rev*, **136**, 1778–1791, <https://doi.org/10.1175/2007MWR2218.1>.

- United States Geological Survey, 2020: Emergency assessment of post- fire debris-flow hazards. .
- Valladares, F., and R. W. Pearcy, 1997: Interactions between water stress, sun-shade acclimation, heat tolerance and photoinhibition in the sclerophyll *Heteromeles arbutifolia*. *Plant Cell Environ*, **20**, 25–36, <https://doi.org/10.1046/j.1365-3040.1997.d01-8.x>.
- Wan, Z., 2014: New refinements and validation of the collection-6 MODIS land-surface temperature/emissivity product. *Remote Sens Environ*, **140**, 36–45, <https://doi.org/10.1016/j.rse.2013.08.027>.
- , Y. Zhang, Q. Zhang, and Z.-L. Li, 2002: *Validation of the land-surface temperature products retrieved from Terra Moderate Resolution Imaging Spectroradiometer data*. [www.elsevier.com/locate/rse](http://www.elsevier.com/locate/rse).
- De Wekker, S. F. J., and M. Kossmann, 2015: Convective boundary layer heights over mountainous terrain—A review of concepts. *Frontiers in Earth Sciences*, **3**, 1–22, <https://doi.org/10.3389/feart.2015.00077>.
- Williams, A. P., and Coauthors, 2015: Correlations between components of the water balance and burned area reveal new insights for predicting forest fire area in the southwest United States. *Int J Wildland Fire*, **24**, 14–26.
- Zhang, C., Y. Wang, and M. Xue, 2020: Evaluation of an E- $\epsilon$  and three other boundary layer parameterization schemes in the WRF model over the southeast pacific and the Southern Great Plains. *Mon Weather Rev*, **148**, 1121–1145, <https://doi.org/10.1175/MWR-D-19-0084.1>.

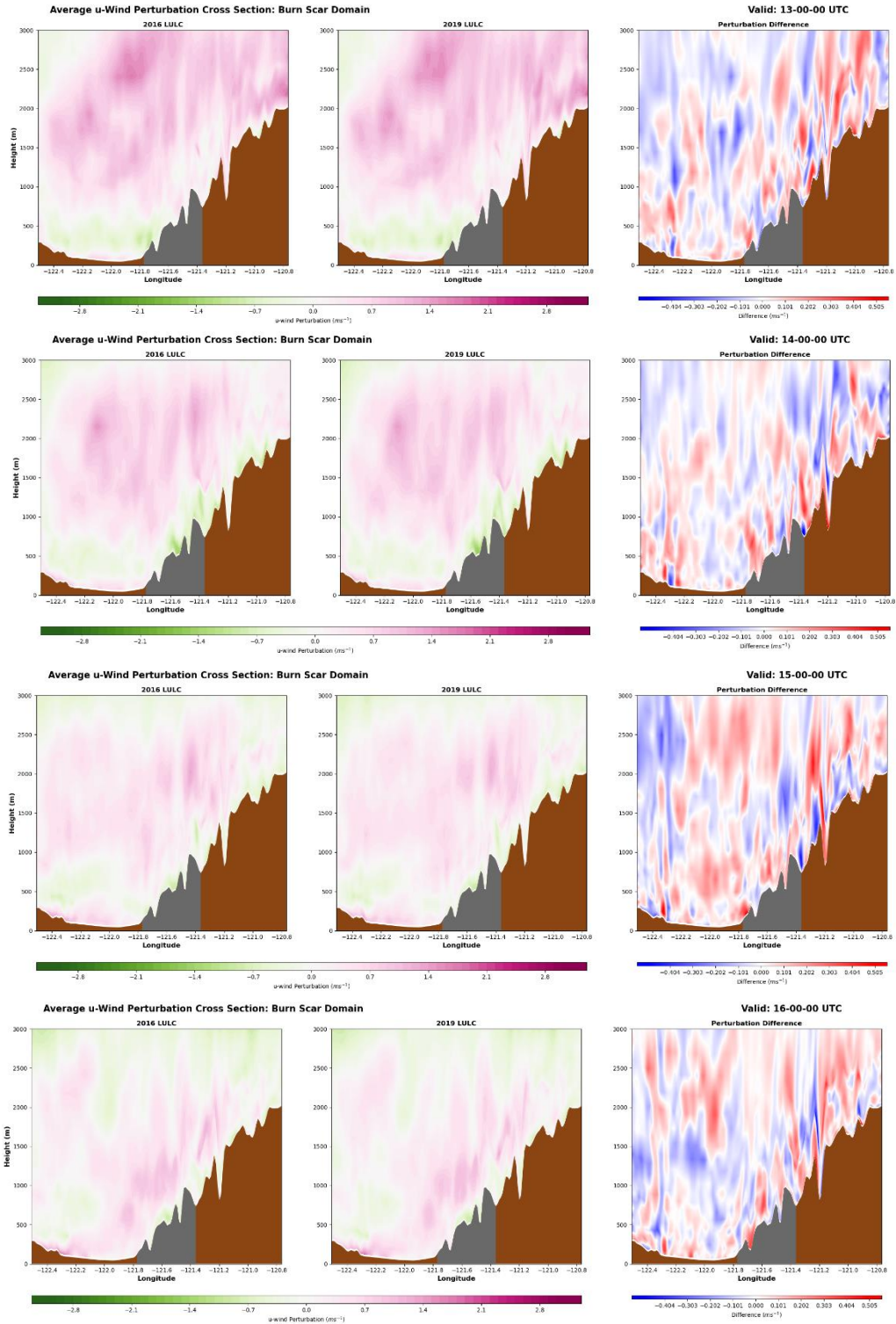
## Appendix A. Statistical Overview of WRF Simulation Results

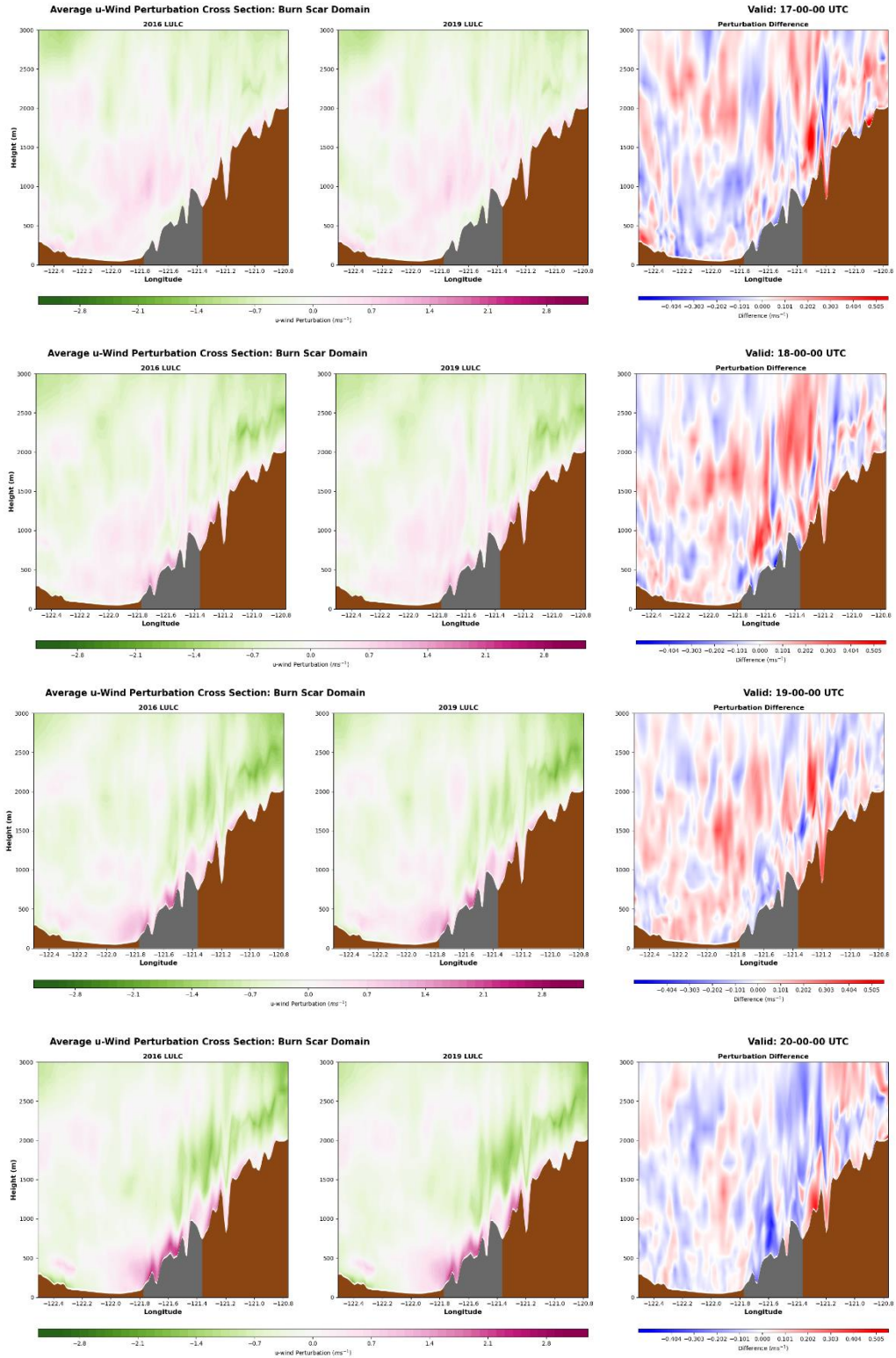
**Table A.1:** Computed statistical results for a selection of variables examined from modeled WRF output. Units for each variable are given in the second column from the left. Statistics averaged from within the burn scar perimeter are reported first in the cell, followed in parentheses by statistics averaged from outside of the burn scar perimeter (subset to domain 3).

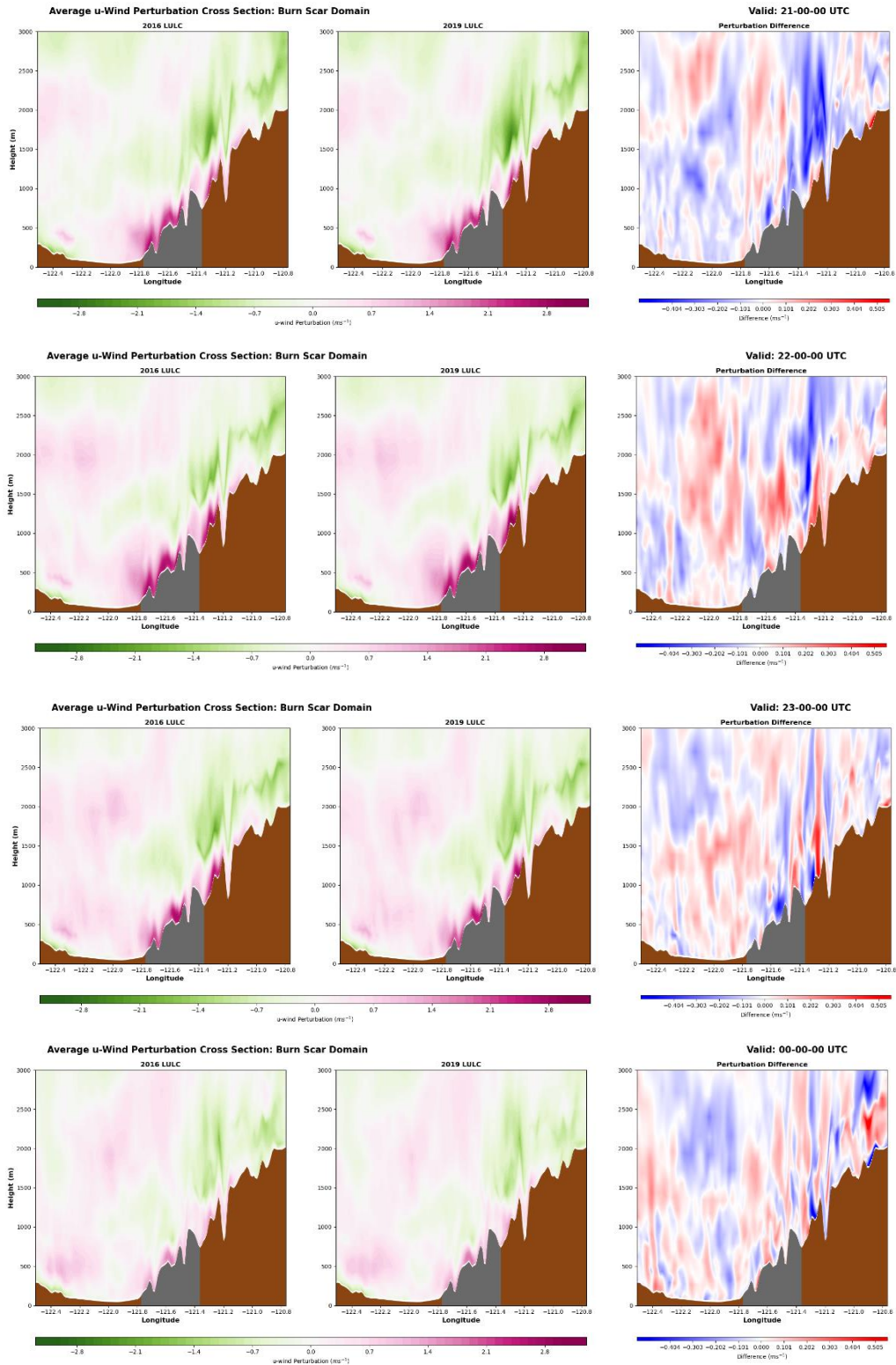
<i>Variable</i>	<b>Units</b>	<b>Mean Difference</b>	<b>Maximum Difference</b>	<b>Minimum Difference</b>	<b>Standard Deviation</b>	<b>P-Value</b>	<b>T Stat</b>
<b>Albedo</b>	-	0.0157 (0.0000)	0.1373 (0.0373)	-0.1267 (-0.0373)	0.0460 (0.0074)	0.0004	3.9368
<b>Emissivity</b>	-	-0.0019 (<0.0001)	0.0900 (0.0303)	-0.0800 (-0.0303)	0.0176 (0.0059)	0.2268	-1.2815
<b>Soil Moisture</b> <small>(avg. over all levels)</small>	cm <sup>3</sup> cm <sup>-3</sup>	-0.0811 (-0.0001)	0.0725 (0.2724)	-0.7295 (-0.2445)	6.2233 (0.0102)	0.8605	-0.1519
<b>LST</b> <small>(full diurnal cycle)</small>	K	0.0867 (-0.0075)	7.7399 (1.8011)	-3.7116 (-1.4445)	0.8821 (0.1695)	0.2297	1.2377
<b>LST Day</b> <small>(16-00 UTC)</small>	K	0.2712 (-0.0104)	9.4404 (2.3730)	-5.0610 (-2.0047)	1.2135 (0.2428)	0.0191	2.6837
<b>LST Night</b> <small>(13-16; 00-13 UTC)</small>	K	-0.2654 (-0.0021)	4.4923 (0.7083)	-4.5816 (-1.0232)	0.5510 (0.0654)	<0.0001	-5.5390
<b>Green Fraction</b>	%	-9.5634 (0.0285)	24.2144 (7.5343)	-52.1657 (-7.4639)	15.4558 (0.5441)	<0.0001	-7.2958
<b>Latent Heat</b>	W m <sup>-2</sup>	-1.5447 (-0.0101)	78.3403 (14.2805)	-33.8110 (-10.3978)	9.2418 (1.0871)	0.0719	-1.9261
<b>Sensible Heat</b>	W m <sup>-2</sup>	2.4154 (0.0044)	59.7792 (9.5066)	-29.5262 (-9.0917)	6.6076 (0.9512)	0.0007	4.2431
<b>Total Net Radiation</b>	MJ m <sup>-2</sup>	-0.1832 (0.0035)	1.5905 (0.9983)	-3.0300 (-1.3262)	0.4601 (0.1425)	<0.0001	-4.6610
<b>2m Temp.</b> <small>(full diurnal cycle)</small>	K	0.1165 (-0.0080)	2.6603 (1.1112)	-2.2436 (-0.9152)	0.5256 (0.1115)	0.0168	2.7394
<b>2m Temp.</b> <small>(Day: 16-00 UTC)</small>	K	0.2211 (-0.0102)	3.8102 (1.5203)	-3.0339 (-1.3623)	0.7549 (0.1601)	0.0037	3.5410
<b>2m Temp.</b> <small>(Night: 13-16; 00-13 UTC)</small>	K	-0.2831 (-0.0039)	1.1850 (0.3301)	-1.7715 (-0.5047)	0.1978 (0.0390)	0.0003	-4.6306
<b>2m Dewpoint</b>	K	-0.1923 (-0.0064)	3.6918 (1.9301)	-3.1782 (-1.7580)	0.3642 (0.1156)	<0.0001	-6.2645
<b>Surface Pressure</b>	hPa	-0.0082 (0.0018)	0.1483 (0.1434)	-0.2044 (-0.1429)	0.0323 (0.0101)	0.0040	-3.5302
<b>10m U-Wind</b>	ms <sup>-1</sup>	-0.0755 (-0.0019)	0.2443 (0.8006)	-0.5793 (-0.5902)	0.1502 (0.0426)	<0.0001	-5.6373
<b>10m V-Wind</b>	ms <sup>-1</sup>	-0.0590 (-0.0034)	0.5849 (0.3582)	-0.6879 (-0.4330)	0.1518 (0.0439)	0.0043	-4.2224
<b>10m Wind</b>	ms <sup>-1</sup>	0.1152 (0.0019)	1.2712 (0.5753)	-0.6908 (-0.8136)	0.2227 (0.0547)	<0.0001	5.8669
<b>U*</b>	ms <sup>-1</sup>	-0.0122 (0.0002)	0.2761 (0.06691)	-0.3491 (-0.1157)	0.0705 (0.0086)	0.0501	-2.0388

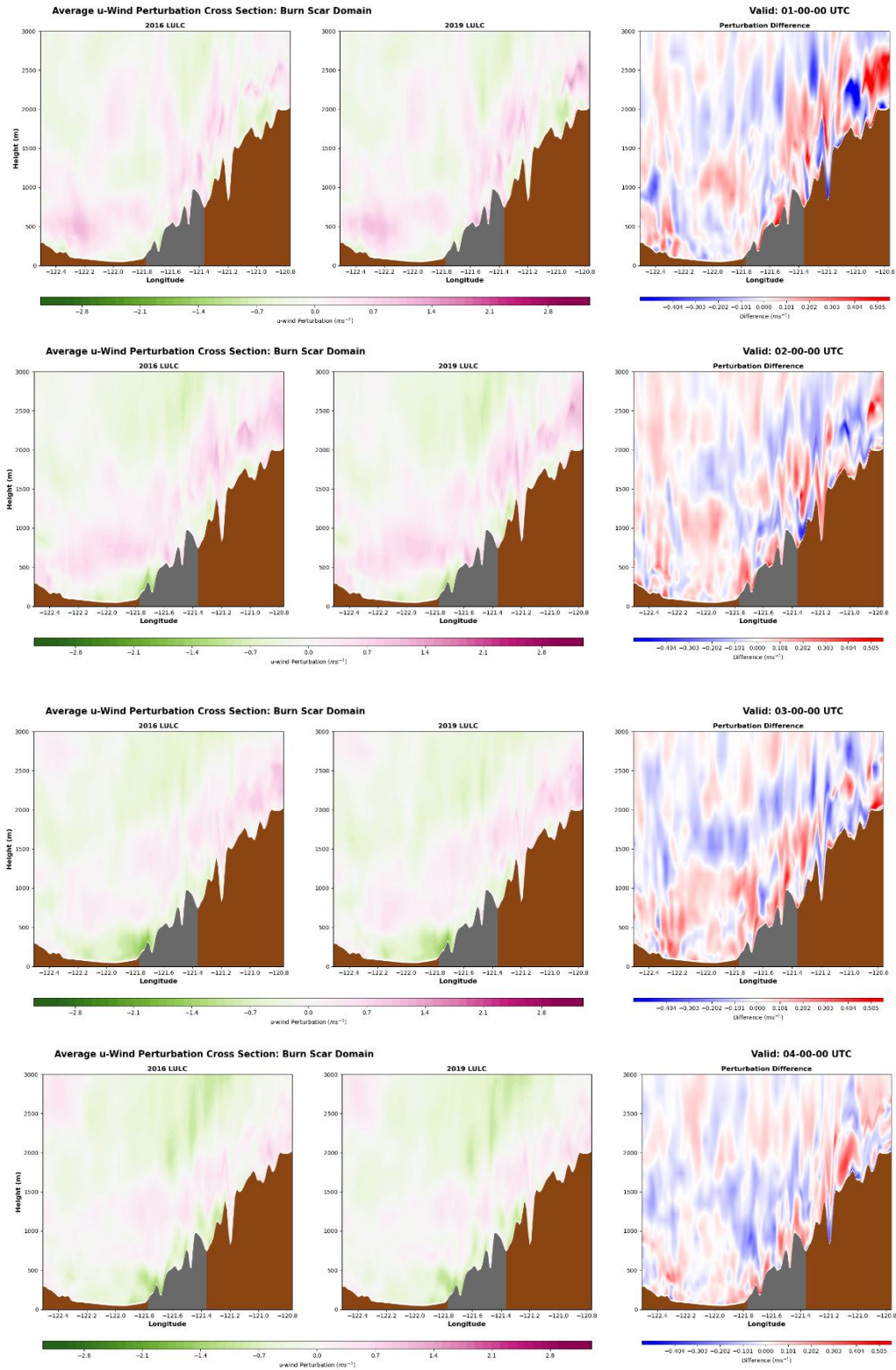
<b>10m Wind Divergence</b>	10 <sup>-4</sup> s <sup>-1</sup>	10.6771 (-1.2968)	2022.4647 (2352.5544)	-2055.7937 (-3367.4077)	405.0285 (207.4057)	0.6223	0.3331
<b>Precipitation</b>	mm	-0.0241 (-0.0333)	1.3269 (9.0582)	-1.8917 (-8.0127)	0.4013 (0.8050)	0.2633	0.2498
<b>Total Cld. Frac.</b>	%	0.0844 (-0.0004)	1.2747 (2.6946)	-0.8440 (-2.2582)	0.3856 (0.2837)	0.0891	3.1426
<b>Low Cld. Frac.</b>	%	0.2305 (0.0682)	0.7440 (1.1510)	-0.2595 (-1.4974)	0.2186 (0.1604)	0.0006	9.9833
<b>Middle Cld. Frac.</b>	%	0.1227 (0.0545)	0.4786 (0.8282)	-0.2550 (-0.9018)	0.1865 (0.1235)	0.1026	5.2534
<b>High Cld. Frac.</b>	%	-0.0002 (0.0006)	0.0766 (0.1110)	-0.0849 (-0.1534)	0.0310 (0.0319)	0.1510	-3.0169

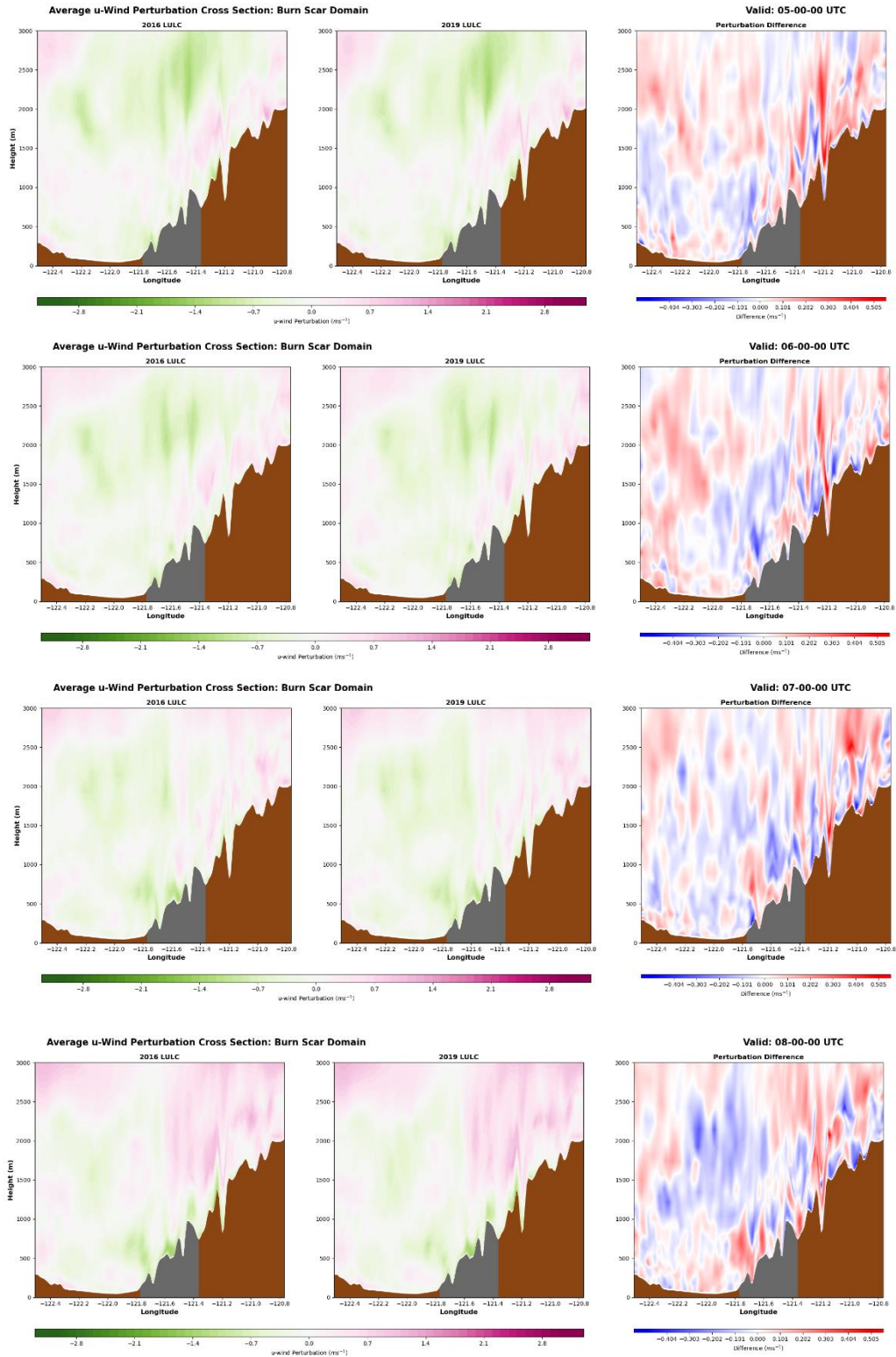
# Appendix B. WRF Simulation Average U-Wind Perturbations

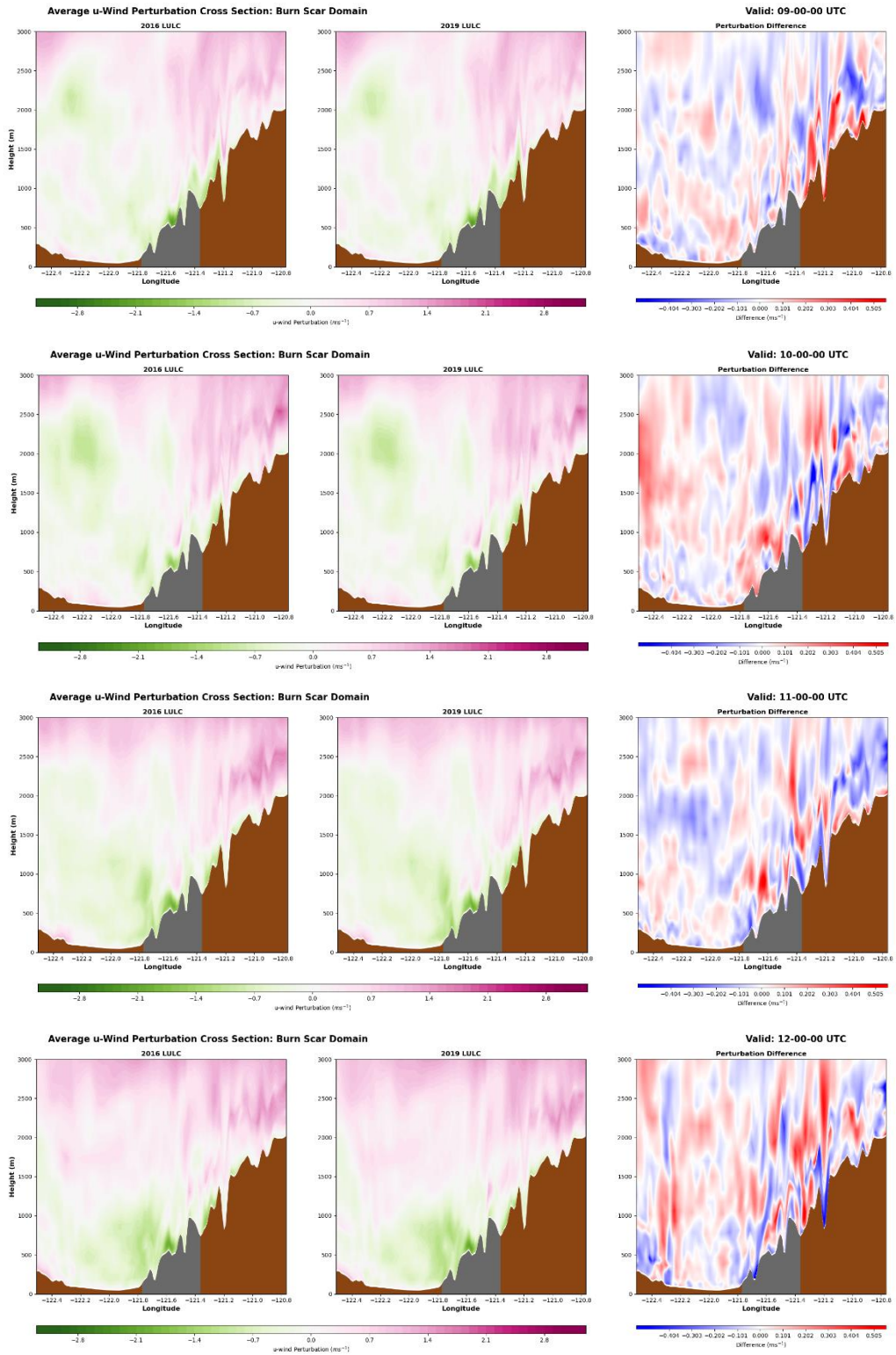












**Figure B.1:** x-z cross section analysis of run-averaged u-wind perturbations. Each hour of the diurnal cycle is shown for the innermost WRF domain.